AGU PUBLICATIONS

Journal of Advances in Modeling Earth Systems

RESEARCH ARTICLE
10.1002/2015MS000537

The Stochastic Parcel Model: A deterministic parameterization of stochastically entraining convection

David M. Romps[1,2]

[1]Department of Earth and Planetary Science, University of California, Berkeley, California, USA, [2]Climate and Ecosystem Sciences Division, Lawrence Berkeley National Laboratory, Berkeley, California, USA

Key Points:
- The SPM is a convective parameterization based on Poisson-process entrainment
- The SPM groups updrafts by their purity to achieve computational efficiency
- The SPM is implemented in a single-column model and compared with an LES

Correspondence to:
D. M. Romps,
romps@berkeley.edu

Citation:
Romps, D. M. (2016), The Stochastic Parcel Model: A deterministic parameterization of stochastically entraining convection, *J. Adv. Model. Earth Syst.*, *8*, 319–344, doi:10.1002/2015MS000537.

Received 21 AUG 2015
Accepted 26 FEB 2016
Accepted article online 1 MAR 2016
Published online 16 MAR 2016

Abstract Convective entrainment is a process that is poorly represented in existing convective parameterizations. By many estimates, convective entrainment is the leading source of error in global climate models. As a potential remedy, an Eulerian implementation of the Stochastic Parcel Model (SPM) is presented here as a convective parameterization that treats entrainment in a physically realistic and computationally efficient way. Drawing on evidence that convecting clouds comprise air parcels subject to Poisson-process entrainment events, the SPM calculates the deterministic limit of an infinite number of such parcels. For computational efficiency, the SPM groups parcels at each height by their purity, which is a measure of their total entrainment up to that height. This reduces the calculation of convective fluxes to a sequence of matrix multiplications. The SPM is implemented in a single-column model and compared with a large-eddy simulation of deep convection.

1. Introduction

Within the climate-modeling community, there is a widely recognized and urgent need to improve representations of convective entrainment [e.g., *Hirota et al*., 2014]. According to several studies, the convective entrainment rate, when varied over its range of uncertainty, is the one parameter that exerts the most influence on a global climate model's (GCM's) climate sensitivity [*Knight et al*., 2007; *Sanderson et al*., 2008; *Rougier et al*., 2009; *Klocke et al*., 2011]. In addition, studies have documented how different choices of the entrainment rate have dramatic influences on atmospheric humidity [*Siebesma and Holtslag*, 1996], cloud cover [*Jakob and Siebesma*, 2003], patterns of precipitation [*Chikira*, 2010], radiative fluxes [*Held et al*., 2007], intraseasonal variability [*Tokioka et al*., 1988], and interseasonal variability [*Watanabe et al*., 2011].

Current convective parameterizations rely on a variety of ad hoc choices to represent entrainment. Some of these choices, such as the common use of a single entraining updraft [e.g., *Kain and Fritsch*, 1990; *Zhang and McFarlane*, 1995], were made for reasons of algorithmic simplicity and computational efficiency. Other choices, such as the use of an adiabatic plume rising through the depth of the troposphere [e.g., *Raymond and Blyth*, 1986; *Emanuel*, 1991], were made for lack of observations or large-eddy simulations to contradict them. In the past several years, however, much has been learned about convective entrainment, including insights on the important role of heterogeneous updraft properties in tracer transport [*Lawrence and Rasch*, 2005; *Romps*, 2010] and the dearth of undiluted deep convection in cloud-resolving simulations [*Kuang and Bretherton*, 2006; *Fierro et al*., 2009; *Romps and Kuang*, 2010a].

A particularly useful insight, which motivates the scheme described here, comes from the work of *Romps and Kuang* [2010a]. In that study, a "purity" tracer was used to study entrainment in a large-eddy simulation of deep convection. The purity tracer is a passive tracer within convecting clouds, but it has sources and sinks elsewhere that maintain its mixing ratio ϕ at one in the subcloud layer and zero in the nonconvecting parts of the free troposphere. The purity ϕ of an updraft, therefore, records the fraction of the updraft's dry air mass that came directly from the subcloud layer. *Romps and Kuang* [2010a] showed that the mass flux of "undiluted" updrafts (defined as updrafts with a purity above 0.8) decays exponentially with height. This was explained as updrafts being subjected to Poisson-process mixing events generated by the turbulent flow. In particular, if each parcel of updraft air has a probability dz/λ of becoming diluted by entrainment every distance dz that it ascends, then the undiluted mass flux will decay with height with an e-folding distance of λ.

Romps and Kuang [2010b] put this insight to work by developing the Stochastic Parcel Model (SPM), which we will refer to as the Lagrangian implementation of the SPM (LSPM) when we need to differentiate it from the scheme developed here. In the LSPM, convection is simulated by a large collection of Lagrangian parcels that entrain stochastically. Each parcel evolves in time according to a coupled set of ordinary differential equations governing its height, volume, vertical velocity, water content, etc. Each parcel is simulated in isolation, but is subjected to Poisson-process entrainment events that are calculated using a Monte Carlo method. The integration of each parcel's history is halted once the parcel has reached its own unique level of neutral buoyancy. By simulating many of these parcels (all with the same initial conditions), and then by summing their contributions to the convective mass flux at each height, the LSPM predicts a profile of net convective mass flux. In *Romps and Kuang* [2010b], this scheme was compared against a large-eddy simulation of shallow convection and it performed admirably, showcasing its ability to replicate both the means and variances of updraft properties.

Despite this success, the LSPM is not well suited to be a convective parameterization: depending on the number N of parcels simulated, the LSPM is either too computationally expensive (large N) or too noisy (small N). Because convective mass fluxes are obtained by averaging over the N parcels, each of which has a history determined by stochastic entrainment, *Romps and Kuang* [2010b] had to simulate millions of Lagrangian parcels to obtain distributions of cloud properties that were suitably converged. If implemented as a deterministic convective parameterization in a global climate model (GCM), a comparably large number of these parcel integrations would need to be performed for every time step and grid column, thereby increasing the computational expense of a GCM by an unacceptable amount.

With the LSPM, the only alternative is to accept a large amount of stochastic noise in the convective tendencies for each time step and grid column. This is the approach taken by *Nie and Kuang* [2012a] and *Sušelj et al*. [2013]. In *Nie and Kuang* [2012a], the LSPM was used to simulate a spatially uniform case of shallow convection using $N = 150$ parcels per time step and grid column. In the Eddy-Diffusivity/Mass-Flux (EDMF) model of *Sušelj et al*. [2013], the MF part of EDMF is replaced with an $N = 10$ LSPM. By averaging over a sufficient number of time steps and/or a sufficient number of nearby grid cells, the LSPM can produce nearly deterministic mean profiles of cloud properties despite using such small values of N. But the behavior in any given GCM column for any given time step will be highly stochastic. Although schemes that add stochastic noise to GCMs are currently in vogue, the noise generated by the LSPM with a small N is neither intentional nor desirable: this noise stems from the unintentional underresolving of the distribution of properties within turbulent clouds, and the stochastic forcing that this adds to the GCM is an undesirable function of both GCM grid size and time step.

This paper presents an implementation of the SPM that approximates the deterministic $N \to \infty$ limit in a computationally efficient way. When we need to differentiate this from the LSPM, we will refer to this as the Eulerian implementation of the SPM (ESPM). When there is no risk of confusion, we will refer to either one as "the SPM" since the LSPM and ESPM are just two ways of calculating the same thing: the LSPM was intended by *Romps and Kuang* [2010b] to be operated in the large-N limit and the ESPM developed here approximates that large-N limit.

The ESPM approximates the large-N limit by taking advantage of the fact that updraft properties are well correlated with purity. For shallow convection, this correlation can be seen from *Romps and Kuang* [2010b, Figures 3 and 4, right], which show that, at a given height, about 90% of the variance in updraft buoyancy is explained by updraft purity. Figure 1 in this paper shows the profiles of R^2 between purity and three quantities—vertical velocity w, temperature T, and total water mass fraction q_t—in updrafts in a large-eddy simulation of deep convection, which will be described in section 8. Through most of the troposphere, about 50%–80% of the variance in these quantities is explained by the purity alone. The biggest exception is the R^2 between temperature and purity in the upper troposphere, which dips to zero before rebounding to high values. This kink in the T-ϕ R^2 profile is not really a failure of purity to capture variability, but a switch from a positive correlation to a negative correlation. Below the height of zero R^2, updrafts are warmer than their surroundings, so temperature and purity are positively correlated (i.e., entrainment reduces both purity and temperature). Above the height of zero R^2, updrafts are overshooting and, therefore, colder than their surroundings, so temperature and purity are negatively correlated (i.e., entrainment decreases purity, but increases temperature).

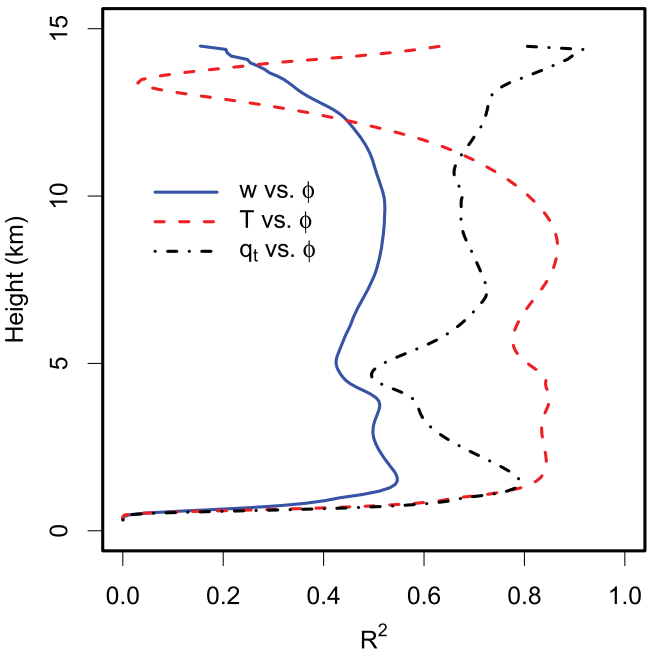

Figure 1. For convective updrafts in a large-eddy simulation of radiative-convective equilibrium, profiles of R^2 between purity ϕ and (blue solid) vertical velocity w, (red dashed) temperature T, and (black dot-dashed) total water mass fraction q_t. Note that purity explains about 50%–80% of the variance through most of the troposphere. See the text for an explanation of the dip in the T-ϕ R^2 profile.

These results suggest that the properties of deep convection can be adequately described by functions of height z and purity ϕ. To visualize this, consider Figure 2 (left), which shows the $\phi(z)$ history for each parcel of an LSPM (depicted as $N = 4$ to avoid clutter). Next, imagine discretizing the height-purity domain, as shown, and then averaging parcel properties within each cell. Since variations in purity explain most of the variations in other parcel properties, averaging the parcel properties within each cell greatly reduces the dimensionality of the output from the LSPM while still preserving most of the information content. This output consists of several matrices, which are discretized functions of ϕ and z. For example, we define one function as the extensive quantity $M(\phi, z)$ such that $M(\phi, z)\, d\phi$ is the mass flux (kg m^{-2} s^{-1}) at height z of updrafts with purity between ϕ and $\phi + d\phi$. We can also define a variety of intensive quantities such as the temperature $T(\phi, z)$ and the specific humidity $q_v(\phi, z)$. The ESPM treats these matrices as a complete description of the convection, and the ESPM generates these matrices for the $N \to \infty$ limit by performing Eulerian calculations directly on this ϕ-z grid rather than mapping Lagrangian parcels to the grid and then averaging.

The ESPM operates by first specifying a closure for the updraft distributions (i.e., M, T, q_v, etc. as functions of ϕ) at the lowest model level above the surface. As we will see in section 5, it is straightforward to formulate a closure for this purpose that is both simple and physical. The more challenging step is calculating the fluxes between cells of the discretized ϕ-z grid (see Figure 2, right) in a way that is consistent with Poisson-process entrainment. The bit of magic is that this can be done semianalytically, reducing the problem to matrix multiplication. The resulting matrix operations can be efficiently performed on a computer, making the ESPM suitable for implementation in global climate models.

2. The SPM in Words

The SPM is a parameterization of ascending convective parcels. While many convective parameterizations include downdrafts, studies using large-eddy simulations have found that downdrafts are not very prevalent [*Lin and Arakawa*, 1997; *Heus et al.*, 2008; *Böing et al.*, 2014] and even the impact of downdrafts on the thermodynamics of the subcloud layer is weak [*Thayer-Calder and Randall*, 2015]. Arguably the most important effect of downdrafts is their generation of cold pools, which generate thermodynamic variance in the boundary layer [*Tompkins*, 2001; *Zuidema et al.*, 2012], trigger new convection through mechanical forcing [*Jeevanjee and Romps*, 2015; *Torri et al.*, 2015], make wide updrafts capable of convecting deeply [*Khairoutdinov and Randall*, 2006; *Böing et al.*, 2012], and even prevent convective self-aggregation [*Jeevanjee and Romps*, 2013]. For simplicity, however, downdrafts and cold pools are ignored in the simple closure used here, which is described in section 5.

The Eulerian implementation of the SPM generates a set of matrices that describe the ensemble of ascending parcels at a given location (e.g., GCM grid column) and a given time (e.g., GCM time step). The rows and

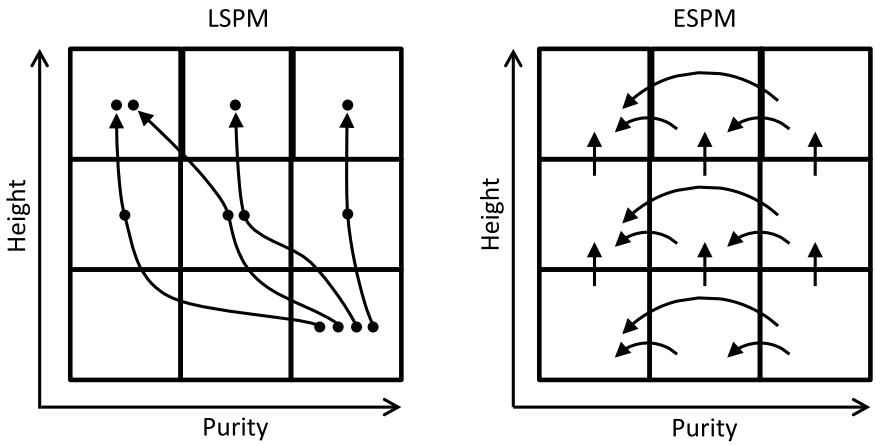

Figure 2. (left) The Lagrangian trajectories, shown by arrows in ϕ-z space, that are calculated by the LSPM. (right) The Eulerian fluxes, shown by arrows in ϕ-z space, that are calculated by the ESPM.

columns of these matrices correspond to height and purity, respectively. The rows represent heights that, in a typical application, are chosen to range from the surface to the lower stratosphere; these are the heights at which the mass fluxes are defined. The columns correspond to adjacent, nonoverlapping bins covering a dimensionless interval from zero to one; each of these bins defines the purity of the parcels within that column. The SPM generates one matrix for the extensive quantity of mass flux and several matrices for the various intensive quantities such as moist static energy, specific humidity, and vertical velocity.

For example, an element of the mass-flux matrix M gives the updraft mass flux per purity interval (i.e., ∂[mass flux]/$\partial\phi$) within the corresponding purity range (defined by the column) and at a specific height (defined by the row). A row of the M matrix gives the distribution of mass flux per purity interval at a given height. A column of the M matrix gives the vertical profile of mass flux within that particular purity range. Similarly, an element of the vertical velocity matrix w gives the vertical velocity of parcels at the chosen height and purity range; a row of w gives the vertical velocity of parcels as a function of purity at that height; and a column of w gives the vertical profile of parcel vertical velocity within the corresponding purity range.

Schematically, these matrices are calculated as depicted in Figure 3. First, a closure scheme (described in section 5) is chosen to initialize the first row of all the matrices. This specifies the mass flux and intensive properties of the parcels at a height near the surface. Since parcels begin with unit purity, only the last element of the first row of each matrix needs to be defined by the closure, as shown in step 1 of Figure 3. In other words, the closure needs only to specify the mass flux and intensive properties of a single bulk plume near the surface, and this information gets populated into a single element of each matrix. The other elements of the first row of the M matrix are set to zero. The other elements of the first row of the intensive matrices need not be defined because the mass flux is zero there; matrix elements that are undefined (either because the mass flux is zero or because they are in a row that has not yet been calculated) are shaded grey in Figure 3.

In step 2, the second row of each matrix is populated from the data in the first rows of the matrices using the physical processes of adiabatic ascent, Poisson-process entrainment, and detrainment of negatively buoyant parcels. The equations describing these calculations are given in sections 3 and 4, and the numerical implementation is given in Appendix A. If the probability of an entrainment event between the first and second rows is 30% (i.e., $dz/\lambda = 0.3$), then 30% of the convecting parcels experience entrainment and move to lower-purity bins, i.e., they populate the other columns. In step 2 of Figure 3, we see that some of the mass flux has, indeed, moved to a lower-purity bin. The MSE of that bin is lower than the MSE of the $\phi=1$ bin because those parcels have entrained environmental air with a lower MSE. Next, if a purity bin has negative buoyancy, then parcels in that bin are detrained, which is accomplished by diverting mass flux from that bin into the environment, thereby reducing the bin's mass flux. This is consistent with the concept of buoyancy sorting [*Telford*, 1975; *Taylor and Baker*, 1991], with detrainment of negatively buoyant parcels and the continuing ascent of positively buoyant parcels.

In subsequent steps, this procedure simply repeats. Since an individual parcel can move only upward in height to lower-purity values, the matrix elements in row i and column j depend only on the elements in

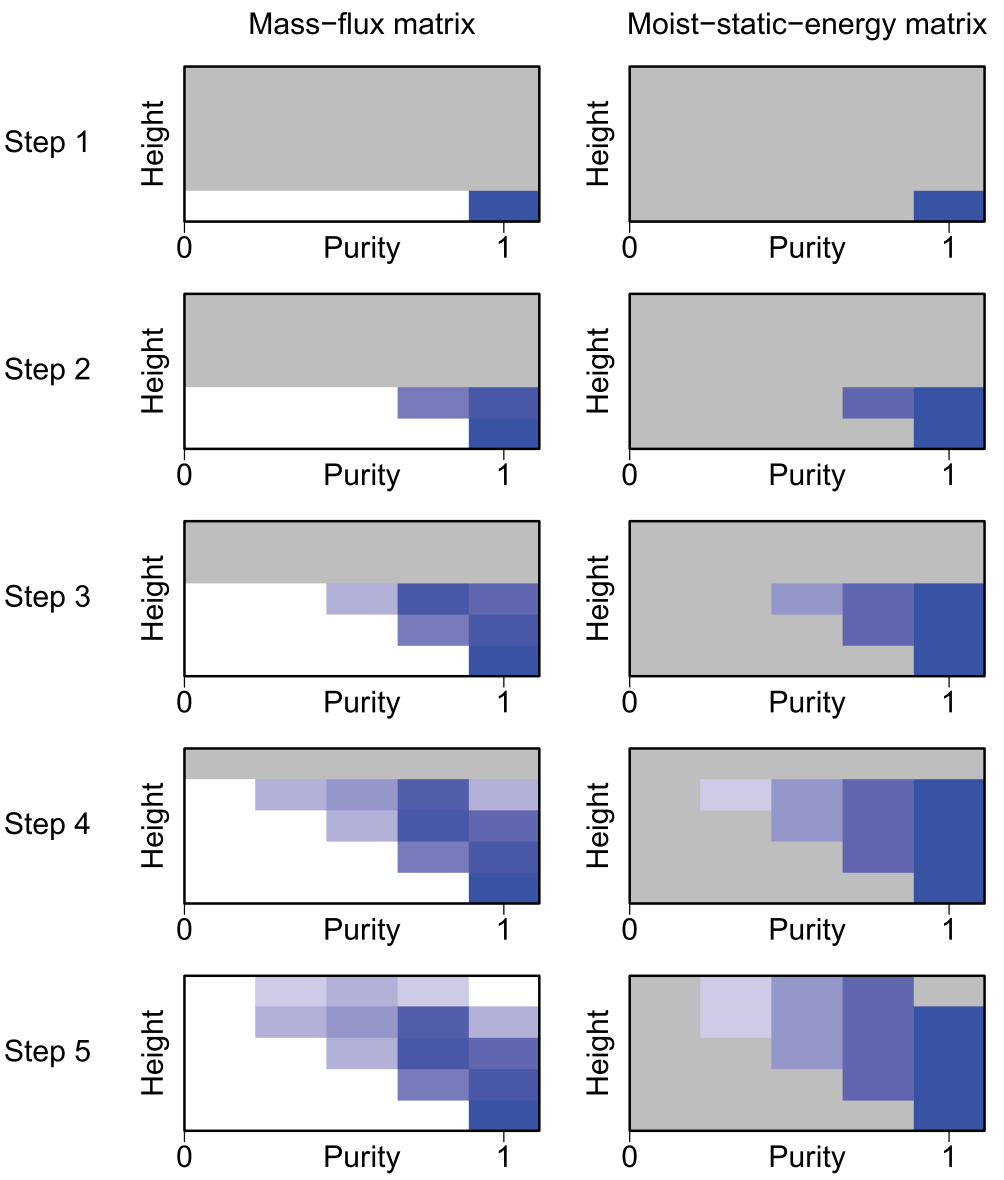

Figure 3. A cartoon illustration of a numerical integration of (left) the mass-flux matrix *M* and (right) the moist-static-energy matrix *h*. Dark blue denotes matrix elements with high values, light blue denotes low values, and grey denotes undefined matrix elements. In this example, there are five purity bins and five height bins. In step 1, the closure specifies the distribution of mass flux in the $\phi=1$ bin at the first height level and the value of moist static energy there. In step 2, the distribution of mass flux and moist static energy at the second height level are calculated from the distributions at the first level by subjecting them to adiabatic ascent, Poisson-process entrainment, and detrainment of negatively buoyant parcels. Proceeding in this way, step 3 calculates the distributions at the third height from the distributions at the second height, and so on.

row $i-1$ and columns j to N_ϕ, where N_ϕ is the total number of columns. Furthermore, as in the original LSPM, the parcels are assumed to be noninteracting. This simplifies the equations and the resulting discretization because it implies that the parcel properties in row i are *linear* functions of the parcel properties in row $i-1$. Therefore, as shown in Appendix A, each row i of mass-flux matrix M is calculated by multiplying row $i-1$ of M by an appropriately defined matrix, and similarly for all of the intensive matrices. Therefore, this new Eulerian implementation of the SPM reduces a computationally daunting challenge—calculating the infinite spectrum of parcels generated by Poisson-process entrainment events—to a series of computationally efficient matrix multiplications.

Once these matrices have been constructed, the total updraft mass flux at each height (i.e., at each row) is given by a weighted sum over the columns of M, where the weights are the sizes of the purity bins (recall

that each element of M is the differential mass flux per differential purity interval). The profile of convective MSE flux is given by taking the Hadamard product (i.e., the entrywise product) of mass-flux matrix M and MSE matrix h and then taking the weighted sums over the columns, again weighting by the sizes of the purity bins. In this way, the total convective flux of any quantity can be calculated. By taking the vertical derivative of these flux profiles, we obtain tendencies that can be fed back to a GCM.

It is important to emphasize that the Stochastic Parcel Model is deterministic. It is currently popular to add intentional random noise to parameterizations for GCMs, and these schemes are often referred to as "stochastic." The SPM, while it has "stochastic" in its name, is not one of those schemes. The SPM is a model of convecting parcels that entrain stochastically, but the matrices and tendencies produced by the SPM describe the deterministic $N \to \infty$ limit of N such parcels.

Finally, note that the ESPM is not a spectral-plume model. There is some risk of confusion on this point because the output of the ESPM is given by matrices on axes of z and ϕ (which quantifies entrainment), while the output of a spectral-plume model [e.g., *Arakawa and Schubert*, 1974] can be represented by matrices on axes of z and the fractional entrainment rate (which distinguishes between the different plumes). Any similarities, however, end there. In a spectral-plume model, all of the convective variability is baked into the lowest level, where the mass flux for each entraining plume is set by a CAPE-like closure; in the ESPM, there is zero convective variability at the lowest level. In a spectral-plume model, the mass-flux profile is defined by the CAPE-like closure imposed at the cloud base; in the ESPM, the mass-flux profile is determined by buoyancy sorting in the free troposphere. In a spectral-plume model, each plume evolves in height in a completely deterministic fashion; in the ESPM, each parcel evolves in height in a completely stochastic fashion. In a spectral-plume model, each column of a matrix corresponds to a single plume, so each column can be calculated independently; in the ESPM, parcels move between columns (as they entrain and change their purity), so it is impossible to calculate a single column in isolation.

3. Mathematical Formulation

Let $M(\phi, z)\, d\phi$ be the flux of mass at height z with purity in the range of $[\phi, \phi+d\phi]$. From height z to height $z + dz$, the fraction of the mass flux that experiences entrainment is dz/λ. Therefore, the change in $M(\phi, z)\, d\phi$ due to parcels with purity in $[\phi, \phi+d\phi]$ entraining is $-M(\phi, z)\, d\phi\, dz/\lambda$. This is an entrainment sink for $M(\phi, z)\, d\phi$. There is also an entrainment source for $M(\phi, z)\, d\phi$, which is caused by mass flux with $\phi' > \phi$ entraining just the right amount of environmental air to have a new purity in $[\phi, \phi+d\phi]$. This calculation is the trickiest part of the ESPM's formulation, so we will go through the logic step by step here.

Consider a parcel of air with purity ϕ' that entrains environmental air with zero purity. Let us denote by χ the ratio of the entrained mass of environmental air to the parcel's initial mass. We will call χ the entrainment fraction. After it entrains, the parcel has a new purity ϕ given by

$$\phi = \frac{\phi'}{1+\chi}\,. \tag{1}$$

We can solve this equation for χ in terms of ϕ' to get

$$\chi = \frac{\phi'}{\phi} - 1\,. \tag{2}$$

In other words, for air with purity ϕ', equation (2) gives the entrainment fraction needed to generate air with purity ϕ. Let us denote by $f(\chi)d\chi$ the probability that, in an entrainment event, the entrainment fraction will lie within $[\chi, \chi+d\chi]$. The function f will be set to an exponential distribution in a moment, but it can be left arbitrary for now. For a parcel with purity ϕ' that entrains, the probability that the parcel's new purity will lie within $[\phi, \phi+d\phi]$ is

$$f(\chi)\left|\frac{\partial \chi}{\partial \phi}\right| d\phi\,.$$

Alternatively, we can think of this as the fraction of the entraining mass flux with a pre-entrainment purity ϕ' that ends up with a post-entrainment purity in $[\phi, \phi+d\phi]$. The amount of mass flux within $[\phi', \phi'+d\phi']$ that entrains between z and $z + dz$ is

$$d\phi' M(\phi', z) \frac{dz}{\lambda} .$$

Therefore, the product of these two expressions gives the mass flux at z within $[\phi', \phi'+d\phi']$ that entrains between z and $z + dz$ and ends up in $[\phi, \phi+d\phi]$. Since each parcel that entrains increases its mass by a factor of $1 + \chi$, the mass flux added to $[\phi, \phi+d\phi]$ within $[z, z + dz]$ from mass flux in $[\phi', \phi'+d\phi']$ at z is

$$d\phi' M(\phi', z) \frac{dz}{\lambda} (1+\chi) f(\chi) \left| \frac{\partial \chi}{\partial \phi} \right| d\phi .$$

Putting it all together, we get

$$\frac{\partial}{\partial z} M(\phi, z) = -\frac{M(\phi, z)}{\lambda} + \int_0^1 d\phi' \, \frac{M(\phi', z)}{\lambda} (1+\chi) f(\chi) \left| \frac{\partial \chi}{\partial \phi} \right| , \tag{3}$$

where $\chi = \phi'/\phi - 1$.

Note that there are two pieces of parametric input to this equation: the Poisson-process length scale λ, which sets the frequency of entrainment events, and the distribution $f(\chi)$, which sets the amount of environmental air entrained in an entrainment event. The value of λ can be diagnosed from large-eddy simulations, and it has been found to be about 500 m in deep convection (*Romps and Kuang* [2010a], which, unfortunately, used a notation in which λ is the inverse of the λ used here) and about 200 m in shallow trade wind cumuli [*Romps and Kuang*, 2010b]. The correct choice for $f(\chi)$, on the other hand, is not so easily determined.

A simple choice would be $f(\chi) = \delta(\chi - \sigma)$, where δ is the Delta function and σ is the mixing fraction that every parcel experiences during an entrainment event. This is the choice made by *Sušelj et al.* [2013]. This choice, however, leads to a quantization of updraft purities, which is not seen in large-eddy simulations. For example, if we used $f(\chi) = \delta(\chi - \sigma)$ with $\sigma = 1$, then every entrainment event would halve a parcel's purity, leading to updraft purities only equal to 2^{-n} for integer n. Instead, LES reveal a smooth distribution of purities in updrafts. To accommodate this, we need to select a smooth distribution function for $f(\chi)$. As in *Romps and Kuang* [2010b], we choose an exponential distribution,

$$f(\chi) = \frac{1}{\sigma} e^{-\chi/\sigma} . \tag{4}$$

Here the constant σ is the mean entrainment fraction experienced by a parcel during an entrainment event. With this structural choice for f, the SPM has two main parameters: λ and σ. As shown in Appendix G, σ/λ is the fractional entrainment rate.

Even with $f(\chi)$ specified, equation (3) is not yet a complete description of the SPM: it is missing terms for detrainment and sources/sinks of mass flux (e.g., a sink of mass flux due to precipitation fallout), and it does not tell us how to evolve the intrinsic quantities such as water vapor or vertical velocity. The general SPM governing equation, which is applicable to all extrinsic and intrinsic quantities, is the following:

$$\begin{aligned} \frac{\partial}{\partial z} [M(\phi, z) X(\phi, z)] = &-\frac{M(\phi, z)}{\lambda} X(\phi, z) + \frac{M(\phi, z)}{w(\phi, z)} S_X(\phi, z) - d(\phi, z) X(\phi, z) \\ &+ \int_0^1 d\phi' \, \frac{M(\phi', z)}{\lambda} [X(\phi', z) + \chi X_e(z)] f(\chi) \left| \frac{\partial \chi}{\partial \phi} \right| . \end{aligned} \tag{5}$$

Here $d(\phi, z)$ is the detrainment rate per purity interval in units of kg m^{-3} s^{-1}, X is the intrinsic quantity, and $S_X(\phi, z)$ is the source (or, if negative, sink) due to processes other than detrainment and has units of s^{-1} times the units of X. The SPM integrates eight of these equations to recover matrices for the fluxes of mass ($X = 1$), water vapor ($X = q_v$), water liquid ($X = q_l$), water solid ($X = q_s$), x velocity ($X = u$), y velocity ($X = v$), z velocity ($X = w$), and moist static energy ($X = h$).

4. Detrainment and Sources

We would like to define the detrainment $d(\phi, z)$ such that it is positive only if the buoyancy $b(\phi, z)$ is negative. This is consistent with the notion of buoyancy sorting, whereby only negatively buoyant parcels are detrained. Furthermore, we demand that detrainment prevent bins from simultaneously

having positive mass flux $M(\phi,z)$ and negative vertical velocity $w(\phi,z)$: if a column of the w matrix is approaching zero as we approach some height, the same column of the M matrix must also go to zero at that height, and it is the job of detrainment to enforce this obviously desirable relationship. Furthermore, for numerical reasons, we want to define $d(\phi,z)$ such that it becomes a smooth function of z between the height where $b=0$ and the height where $w=0$. The alternative is to define $d(\phi,z)$ as a delta function where $w(\phi,z)=0$, but this would lead to spiky detrainment and an undesirable dependence on grid spacing.

To find a formulation for $d(\phi,z)$ that satisfies these criteria, let us consider a simple case where there is no entrainment and no sources or sinks of mass other than detrainment. In that case, the SPM governing equations for $M(\phi,z)$ and $w(\phi,z)$ reduce to

$$\frac{\partial}{\partial z}M=-d$$
$$\frac{\partial}{\partial z}(w^2/2)=b\,.$$

Dividing the first equation by M and the second by $w^2/2$, we get

$$\frac{\partial}{\partial z}\log M=-\frac{d}{M}$$
$$\frac{\partial}{\partial z}\log\left(w^2/2\right)=\frac{2b}{w^2}\,.$$

Imagine that $b=0$ at $z=z_0$ and $w=0$ at $z=z_1>z_0$. One way to guarantee that M goes to zero at z_1 is to require that the fractional changes in M and $w^2/2$ are the same, i.e., that $(\partial/\partial z)\log M$ equals $(\partial/\partial z)\log\left(w^2/2\right)$ for $z_0<z<z_1$. Equating the right-hand sides of the two equations above gives

$$d(\phi,z)=-\frac{2M(\phi,z)}{w(\phi,z)^2}b(\phi,z)\mathcal{H}[-b(\phi,z)]\,, \tag{6}$$

where we have added the Heaviside unit step function $\mathcal{H}$ to specify that this detrainment only turn on when b is negative (i.e., for z satisfying $z_0<z<z_1$). With this choice, note that the detrainment rate is proportional to the negative buoyancy, so it ramps up continuously from zero at $z=z_0$. Furthermore, the proportionality of the derivatives of the logarithms of M and $w^2/2$ ensures that M goes to zero at $z=z_1$. Therefore, equation (6) is used as the definition of detrainment in the SPM.

The sources, denoted by S_X in equation (5), are listed in Table 1 for each of the eight matrices integrated by the SPM. The quantities Auto_l and Auto_s represent the autoconversion of updraft liquid to precipitating rain and the autoconversion of updraft ice to precipitating snow, respectively. Note from Table 1 that the mass and momentum of rain and snow are removed from the updrafts immediately upon formation. The quantities Evap and Melt represent the evaporation of updraft liquid to vapor and the melting of updraft ice to liquid, respectively. In the last column of Table 1, the moist static energy h is defined as

$$h=c_{pm}(T-T_{\text{trip}})+(E_{0v}+R_vT_{\text{trip}})q_v-E_{0s}q_s+gz\,,$$

where c_{pm} is the heat capacity of moist air at constant pressure, which is defined in terms of the mass fractions for dry air (subscript a), vapor (v), liquid (l), and solid (s) and their corresponding heat capacities at constant pressure as

$$c_{pm}=q_ac_{pa}+q_vc_{pv}+q_lc_{pl}+q_sc_{ps}\,.$$

The other constants are the specific gas constant of water vapor (R_v), the gravitational acceleration (g), the triple-point temperature ($T_{\text{trip}}=273.16$ K), the difference in specific internal energy between water vapor and liquid at the triple-point temperature (E_{0v}), and the difference in specific internal energy between liquid and solid at the triple-point temperature (E_{0s}). The variables with a subscript e in Table 1 are the environmental values. The reason for the source of MSE (i.e., the nonzero S_h) is that MSE minus CAPE is conserved for adiabatic parcel ascent [*Romps*, 2015], so $dh/dz=-\text{b}$.

The autoconversion rates are specified as

Table 1. The Variables and Sources Used in Equation (5)[a]

Variable	X	X_e	S_X
Mass	1	1	$-\text{Auto}_l - \text{Auto}_s$
Vapor	q_v	q_{ve}	Evap
Liquid	q_l	q_{le}	$\text{Melt} - \text{Evap} - \text{Auto}_l$
Solid	q_s	q_{se}	$-\text{Melt} - \text{Auto}_s$
Velocity in x	u	u_e	$-(\text{Auto}_l + \text{Auto}_s)\, u$
Velocity in y	v	v_e	$-(\text{Auto}_l + \text{Auto}_s)\, v$
Velocity in z	w	w_e	b
MSE	h	h_e	$-bw$

[a]All of these variables are functions of ϕ and z.

$$\text{Auto}_l = \frac{q_l}{q_l+q_s}\frac{\max(0, q_l+q_s-q_0)}{\tau_l}, \quad (7)$$

$$\text{Auto}_s = \frac{q_s}{q_l+q_s}\frac{\max(0, q_l+q_s-q_0)}{\tau_s}, \quad (8)$$

where q_0 is the condensate mass-fraction threshold, τ_l is the autoconversion time scale for liquid, and τ_s is the autoconversion time scale for solid. Evap and Melt are defined implicitly by the requirement that the air not be supersaturated. Let us define $q_v^{*,l}$ as the saturation vapor mass fraction with respect to liquid and $q_v^{*,s}$ the saturation vapor mass fraction with respect to solid. Explicit expressions for these are given in the appendix of *Romps* [2015]. Using the variable ξ to denote a piecewise linear transition from liquid to solid between temperatures of T_{trip} and 240 K,

$$\xi = \begin{cases} 1 & T \le 240 \\ \dfrac{T_{\text{trip}}-T}{T_{\text{trip}}-240} & 240 < T < T_{\text{trip}} \\ 0 & T \ge T_{\text{trip}} \end{cases}, \quad (9)$$

and defining a saturation fraction that interpolates between $q_v^{*,l}$ and $q_v^{*,s}$ in between these two temperatures

$$q_v^* = [1-\xi(T)]q_v^{*,l} + \xi(T) q_v^{*,s}, \quad (10)$$

the sources Evap and Melt are defined implicitly by the following requirements on q_v, q_l, and q_s in terms of the total-water mass fraction $q_t = q_v + q_l + q_s$:

$$q_v = \min(q_t, q_v^*), \quad (11)$$

$$q_l = (1-\xi)\max(0, q_t - q_v^*), \quad (12)$$

$$q_s = \xi \max(0, q_t - q_v^*). \quad (13)$$

This gives cloud updrafts a mixed-phase region between the triple-point temperature and 240 K. The treatment of precipitation fluxes is given in Appendix B.

5. Closure

In the world of convective parameterizations, the "closure" often refers to the scheme that determines the cloud base mass flux [*Yano et al.*, 2013]. There are many different closures in use (see, for example, *Lin et al.* [2015, Table 2], which lists the closures for CMIP5 models), but the most popular are the CAPE-based closures, which set the cloud base mass flux proportional to CAPE or changes in CAPE. This type of closure is used in many popular convective parameterizations, including the Relaxed Arakawa-Schubert scheme [*Moorthi and Suarez*, 1992] and the *Zhang and McFarlane* [1995] scheme.

The allure of CAPE closures is that they give more convection when there is more CAPE, and since convection tends to reduce CAPE, this prevents surface fluxes and large-scale forcing from pushing CAPE to unreasonably large values. Unfortunately, CAPE closures are not supported by theory, observations, or large-eddy simulations. From a theoretical perspective, it has never been articulated why cloudy parcels being born in updrafts at the cloud base, whose abundance sets the cloud base mass flux, should care about their potential buoyancy later in life, which is what determines CAPE. Without a physical process that causes CAPE to induce cloud base mass flux, making cloud base mass flux a function of CAPE violates causality. Indeed, there is no convincing observational evidence that large CAPE is a skillful predictor of convective mass fluxes. To the contrary, observational studies often find a *negative* correlation between CAPE and precipitation rates (i.e., small CAPE when convective mass fluxes are large) [*Thompson et al.*, 1979; *Mapes and Houze*, 1992;

McBride and Frank, 1999; *Davies et al.*, 2013], and this negative correlation is also seen in large-eddy simulations [*Kuang and Bretherton*, 2006].

The approach taken here is to specify the mass flux of dry updrafts (i.e., unsaturated parcels) at the first numerical level above the surface. These dry updrafts are assumed to occupy 50% of the area, with the other 50% occupied by downdrafts. The vertical velocity of the updrafts is set by the buoyancy of environmental parcels lifted from the near-surface air to that first level above the surface. In particular, the specific kinetic energy is set equal to the vertical integral of the linearly interpolated buoyancy between the two levels; this is similar to the closure used by *Gregory and Rowntree* [1990]. All of the parcels are initialized with identical thermodynamic properties, which are set equal to those of the near-surface environmental air.

With this closure, a positive-upward surface buoyancy flux leads to a balance in which there is a slight instability near the surface that drives an SPM mass flux (and compensating subsidence) that carries that buoyancy away from the surface. Through stochastic entrainment, there is a small spread in the thermodynamic and kinematic properties of parcels by the time they approach the cloud base. Through natural feedbacks between convection and the environment, a small amount of convective inhibition develops near the cloud base to throttle back the mass flux by permitting into the free troposphere only those parcels with sufficient buoyancy and vertical velocity. This throttling of the cloud base mass flux by filtering out all but the most buoyant and quickly rising parcels is also seen in large-eddy simulations of shallow and deep convection [*Kuang and Bretherton*, 2006; *Romps and Kuang*, 2010b]. By using a simple buoyancy-driven mass-flux closure near the surface, allowing parcels to stochastically develop a distribution of properties as they rise, and then letting feedbacks between convection and the environment throttle cloud base mass fluxes, we allow the atmosphere to set cloud base mass fluxes in the way it occurs in nature.

Since the near-surface parcels are newborn and have not yet entrained other environmental air, they all have a purity of one. Therefore, we need only specify the parcel properties in the last column of the first row above the surface. Let us denote by z_s the height of the surface air. Letting $z_s + \Delta z$ denote the height of the first row (or level) above the surface, the closure is as follows:

$$M(\phi, z_s+\Delta z)=\frac{1}{2}\rho_e(z_s+\Delta z)w(1,z_s+\Delta z)\delta(\phi-1), \tag{14}$$

$$w(1,z_s+\Delta z)=\sqrt{\Delta z \max\left(0, g\frac{\theta_v(z_s)-\theta_v(z_s+\Delta z)}{\theta_v(z_s)}\right)}, \tag{15}$$

$$q_v(1,z_s+\Delta z)=q_{ve}(z_s), \tag{16}$$

$$q_l(1,z_s+\Delta z)=q_{le}(z_s), \tag{17}$$

$$q_s(1,z_s+\Delta z)=q_{se}(z_s), \tag{18}$$

$$u(1,z_s+\Delta z)=u_e(z_s), \tag{19}$$

$$v(1,z_s+\Delta z)=v_e(z_s), \tag{20}$$

$$h(1,z_s+\Delta z)=h_e(z_s)\,. \tag{21}$$

Note that the values of all of the intrinsic matrices are undefined at Δz for ϕ other than one. Since the mass flux is zero in those matrix elements, the values there of the intrinsic matrices do not affect the SPM governing equation, which is given by equation (5). For this reason, we may think of the undefined elements as being zero.

6. A Single Call to the SPM

Figure 3 gave a cartoon illustration of the SPM matrices, but now we will see what the matrices look like in a real call to the SPM. First, the SPM is coupled to a single-column model and run to radiative-convective equilibrium (RCE); section 8 will give a detailed description of this simulation. For this section, it suffices to note that about 50% of the time steps have a positive mass flux at 5 km, and, of those, we select a time step with the median flux at 5 km to display here. The top-left plot of Figure 4 shows the *M* matrix from that time step. We see that the purity of parcels decreases from one at the surface to a few percent in the

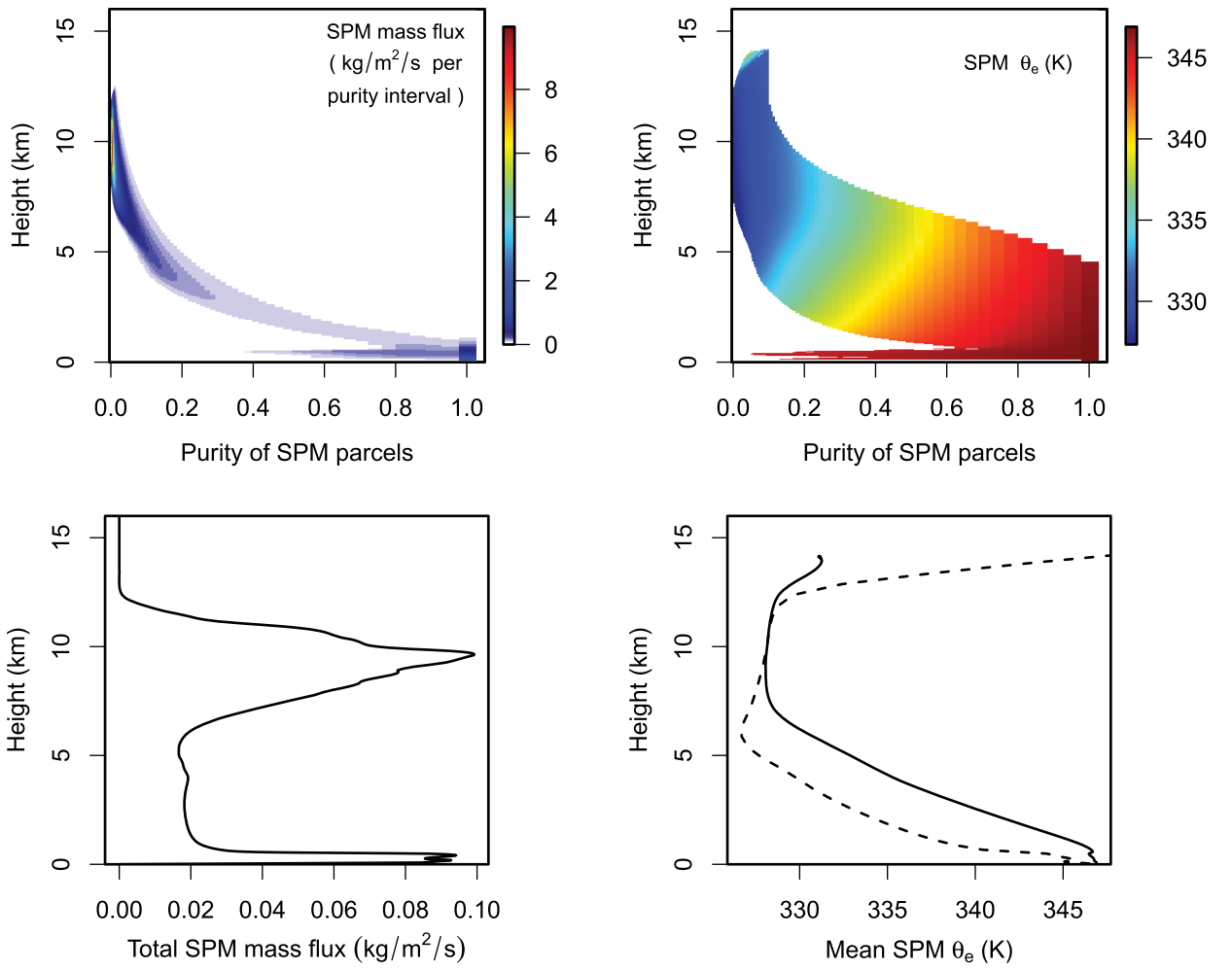

Figure 4. Output from a single call to the SPM, selected as described in the text from a simulation of radiative-convective equilibrium. (top left) The mass-flux matrix $M(\phi, z)$. (bottom left) The mass-flux profile $M(z)$, calculated from $M(\phi, z)$. (top right) The equivalent-potential-temperature matrix $\theta_e(\phi, z)$. (bottom right) (solid) The mass-flux-weighted profile of updraft $\theta_e(z)$, as calculated from $M(\phi, z)$ and $\theta_e(\phi, z)$, and (dashed) the θ_e profile of the single-column model that called the SPM.

upper troposphere. It is encouraging to note that this result resembles that of *Romps and Kuang* [2010a, Figure 3], who used a purity tracer in an LES of RCE to plot the mass flux in a similar way. A noticeable difference here is the mass flux at low purity below the cloud base. This feature appears here, and not in *Romps and Kuang* [2010a], because the purity is set to one only at the first SPM level, whereas *Romps and Kuang* [2010a] set the purity to one everywhere below the cloud base. Another difference is that the mass-flux matrix M records the mass flux of all parcels, whether or not they satisfy the conditions ($w > 1$ m s^{-1} and $q_l + q_s > 10^{-5}$) that *Romps and Kuang* [2010a] used for conditional sampling of the LES. What is particularly interesting about the low-purity boundary layer mass flux in the SPM is that it terminates so abruptly and completely near the cloud base. This is the signature of the cloud base throttle discussed in the previous section: the environmental temperature naturally adjusts to restrict the mass flux at the cloud base so that, in RCE, the latent heating in the free troposphere matches the radiative cooling.

The bottom-left plot of Figure 4 plots the profile of total mass flux, which is given by $M(z) = \int_0^1 d\phi\, M(\phi, z)$. In other words, the mass flux at a particular height is equal to the weighted sum of the appropriate row of M, with weights equal to the width of the purity bins. As we will see in section 8, this instantaneous mass-flux profile closely resembles the time-averaged mass-flux profile, which is too top-heavy. Similarly, the purity values in the upper troposphere are too low. Since *Romps and Kuang* [2010a] diagnosed a λ of 500 m for deep convection, which is larger than the λ of 200 m diagnosed by *Romps and Kuang* [2010b] for shallow

convection, the choice of $\lambda = 250$ m used here is likely too small in the upper troposphere. As shown in section 8, a remedy for the upper-tropospheric mass-flux and purity biases is to make λ increase with height.

The top-right plot of Figure 4 shows the θ_e matrix. Each element of this matrix gives the equivalent potential temperature of convective updrafts at the corresponding height (row) and purity (column). The white areas are where the θ_e of updrafts is undefined because the updraft mass flux is identically zero. There is zero mass flux to the left of the colored region because entrainment generates parcels in that region with such a negative buoyancy and such a small *w* that the parcels reach zero *w* (and, therefore, detrain) before ascending even one grid spacing. There is zero mass flux to the right of the colored region because the numerical implementation of the scheme zeros out trivially small mass fluxes to increase computational efficiency; the mass flux reaches trivially small values at high purity and high altitude because entrainment has subjected the mass flux there to multiple *e*-foldings of decay.

The bottom-right plot of Figure 4 shows the profiles of environmental θ_e and updraft θ_e as the dashed and solid curves, respectively. The profile of environmental θ_e is fed to the SPM when it is called. In a GCM, this would be the instantaneous θ_e of a GCM grid column. Here it is the profile of θ_e from the single-column model, which will be described in section 8. The profile of updraft θ_e is given by $\int_0^1 d\phi\, \theta_e(\phi, z) M(\phi, z)/M(z)$, which is calculated using the two matrices in the top row of Figure 4. Note that this profile cannot be interpreted as the θ_e of any one ascending parcel. Instead, this mean θ_e is an average over parcels with a wide range of purity, including low-purity parcels that have recently had an entrainment event and, due to their negative buoyancy, will soon detrain. In fact, by virtue of having recently entrained (and, therefore, having a large mass), those negatively buoyant and soon-to-detrain parcels have a large influence on mass-flux-weighted updraft properties, just as they do in an LES or observations.

7. Convergence of the SPM

Discretization is a necessary evil in any numerical integration, and the SPM is no exception. In the calculation of the SPM governing equation (5), both the height and the purity are discretized, giving rise to matrices. The height is discretized using a constant Δz spacing, and the purity is discretized logarithmically using a constant $\Delta \log(\phi)$ spacing. If the SPM has been coded in a numerically robust way, then the matrices that it produces will converge as the Δz and $\Delta \log(\phi)$ spacings are taken to zero. Furthermore, the matrices should converge at fairly predictable values of Δz and $\Delta \log(\phi)$, namely $1/\lambda$ and $\sigma/(1+\sigma)$, respectively. For $\Delta z \ll 1/\lambda$ and $\Delta \log(\phi) \ll \sigma/(1+\sigma)$, the matrices should be fully converged. To test this, we take the same time step used to make Figure 4 and we recalculate the mass-flux profile for a variety of Δz and $\Delta \log(\phi)$. The results are shown in Figure 5. The left plot shows the test of Δz convergence, in which $\Delta \log(\phi)$ is held fixed at the small value of 0.05 and Δz is varied from 100 m (red curves) to 1 m (blue curves). The right plot shows the test of $\Delta \log(\phi)$ convergence, in which Δz is held fixed at the small value of 10 m and $\Delta \log(\phi)$ is varied from 0.5 (red curves) to 0.01 (blue curves). In this case, $1/\lambda = 250$ m and $\sigma/(1+\sigma) = 0.2$. As expected, the mass flux has fully converged for values of Δz and $\Delta \log(\phi)$ much less than these respective values.

8. The SPM in RCE

Up to this point, we have motivated the scientific rationale for the SPM, explained how it works, and shown that it converges. In this section, we will implement the SPM in a single-column model and show that it closely replicates an LES. In particular, we will run the SPM and the LES to radiative-convective equilibrium (RCE) and then compare their simulated profiles of temperature and humidity, as well as their updraft properties. We will not undertake any major effort to tune the SPM, or to evaluate it in more complicated cases; such work will be left to future studies.

The large-eddy simulation is run to RCE over an ocean with Das Atmosphärische Modell (DAM) [*Romps*, 2008] on a square doubly periodic domain with a width of 36 km and a model top at 30 km. The sea-surface temperature is set to 300 K, and surface fluxes are calculated using a bulk formula. In the bulk formula, a mean westerly wind of 5 m/s is added to the actual wind speeds. Both shortwave and longwave radiation are calculated interactively using the Rapid Radiative Transfer Model [*Clough et al.*, 2005; *Iacono et al.*, 2008], and the top-of-atmosphere insolation is specified to be a constant diurnal average for the equator on 1 January. The LES grid has a horizontal spacing of $\Delta x = \Delta y = 100$ m and a vertical spacing of

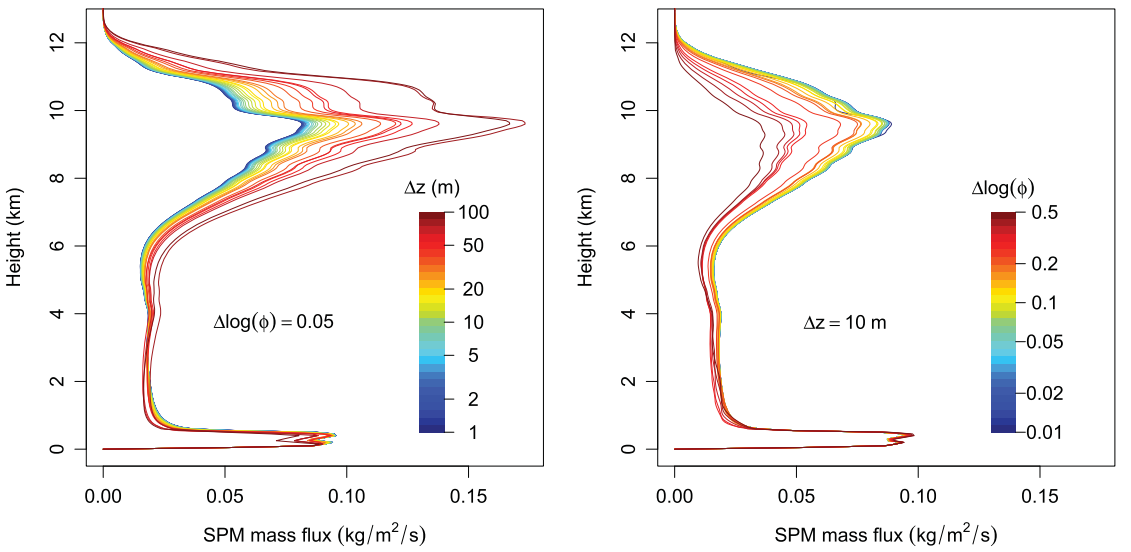

Figure 5. Tests of the convergence of the SPM using the same time step used in Figure 4. (left) Mass-flux profiles using a logarithmic purity grid spacing of $\Delta\log(\phi)=0.05$ and a height grid spacing with Δz ranging from (red colors) 100 m to (blue colors) 1 m. (right) Mass-flux profiles using a height grid spacing of $\Delta z = 10$ m and a logarithmic purity grid spacing with $\Delta \log(\phi)$ ranging from (red colors) 0.5 to (blue colors) 0.01.

$\Delta z = 50$ m for $z < 600$ m, $\Delta z = 100$ m for 1 km $< z <$ 17 km, $\Delta z = 1$ km for $z > 26$ km, and smoothly transitioning in between. The default time step of 5 s is reduced as needed to satisfy the Courant-Friedrichs-Lewy (CFL) condition. The simulation is restarted from a coarser RCE simulation (500 m grid spacing) and is then run for 2 weeks of model time. Statistics are calculated from the last week.

To construct a single-column model with the SPM as the convective parameterization, the SPM is coupled to a single column of DAM. We refer to this pairing as Stochastic PArcel Model In A Column (SPAMIAC). Even though DAM is a large-eddy model, a single column of DAM is dynamically impotent. Only by coupling it to a convective parameterization can the column simulate radiative-convective equilibrium; without a convective parameterization, the column would simulate radiative equilibrium, which has a dramatically different temperature structure.

In SPAMIAC, the coupling between the SPM and DAM is straightforward. The SPM feels DAM through the seven X_e variables listed in Table 1. DAM feels the SPM through the tendencies that the SPM generates, as described in Appendix F. In SPAMIAC's simulation of RCE, DAM uses a 100 s time step and a vertical grid spacing that transitions from 100 m at the surface to 500 m at 5 km, and then transitions from 500 m at 23 km to 1.2 km at 30 km. The surface-flux scheme and radiative forcing are the same as in the LES. In the discretization of SPM's equation (5), which is explained in detail in Appendix A, height z is discretized by subdividing DAM's grid such that the vertical grid spacing Δz does not exceed 100 m, and purity ϕ is discretized into bins that have a common logarithmic spacing of $\Delta\log(\phi)=0.05$. The SPM's height grid extends from the surface to an altitude of 20 km. The purity grid extends from 100% to less than 1%. SPAMIAC is run to RCE for 50 days; statistics are calculated from the last 25 days.

The SPM has seven tunable parameters, which relate to entrainment and microphysics. Regarding entrainment, there are λ (the mean distance between entrainment events) and σ (the mean fraction of environmental air entrained in an entrainment event), which are used in equations (5) and (4), respectively. In this RCE simulation, we use $\lambda = 250$ m and $\sigma = 0.25$, which give a mean entrainment rate of $\sigma/\lambda = 1$ km^{-1}. Regarding microphysics, we have five parameters: the critical condensate mass fraction q_0 and the time scales τ_l and τ_s in the autoconversion equations (7) and (8), and the sedimentation efficiency SE and the evaporation/sublimation e-folding height ζ used in equations (B3) and (B4) of Appendix B. Here we set $q_0 = 5\times10^{-4}$, $\tau_l = 300$ s for temperatures above freezing and $\tau_s = 50$ s for temperature below freezing (i.e., faster generation of precipitation in the mixed-phase region), SE = 0.3, and $\zeta = 3$ km.

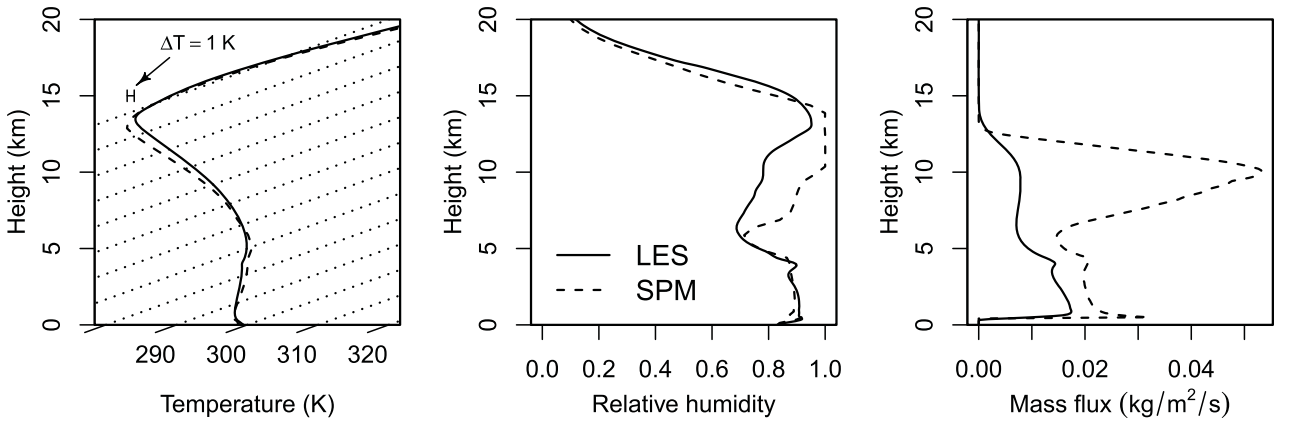

Figure 6. Profiles of (left) temperature, (middle) relative humidity, and (right) mass flux conditioned on $w > 1$ m s^{-1} and $q_l + q_s > 10^{-5}$ for (dashed) the LES RCE simulation, i.e., DAM at 100 m resolution, and (solid) the SPM RCE simulation, i.e., SPAMIAC as described in the text.

Figure 6 shows the profiles of temperature, relative humidity, and updraft mass flux for both the LES and the SPM (the former is DAM run at 100 m resolution, and the latter is SPAMIAC). The SPM generates a temperature profile that is very similar to that generated by the LES. It might sound surprising that a convective parameterization with such a large entrainment rate (1 km^{-1}) could generate the correct lapse rate. For deep convection, the community is used to thinking of entrainment rates as being less than 0.5 km^{-1} [see, for example, *Romps*, 2010, Figure 2]. Those lower effective entrainment rates, however, are generated by shoehorning convection into a bulk-plume model. As discussed by *Romps* [2010], the bulk-plume model underestimates the true entrainment rate because it neglects cloud heterogeneity. In large-eddy simulations, entrainment rates much closer to 1 km^{-1} are found using Eulerian direct measurement [see *Romps*, 2010, Figure 7], and those larger rates have been confirmed by another method of Eulerian direct measurement [*Dawe and Austin*, 2011] and by Lagrangian direct measurement [*Yeo and Romps*, 2013].

The profiles of relative humidity have both similarities and differences. Both the LES and the SPM start at 80% at the surface and then increase to 90% at the cloud base, and they both simulate an RH minimum at a height of about 5 km. In the upper troposphere, however, the SPM is significantly more moist. Both the LES and the SPM have their greatest concentration of ice from anvils at about 11 km, but the mass fraction of ice in the SPM is about 6 times greater there. There are many possible explanations for this difference in

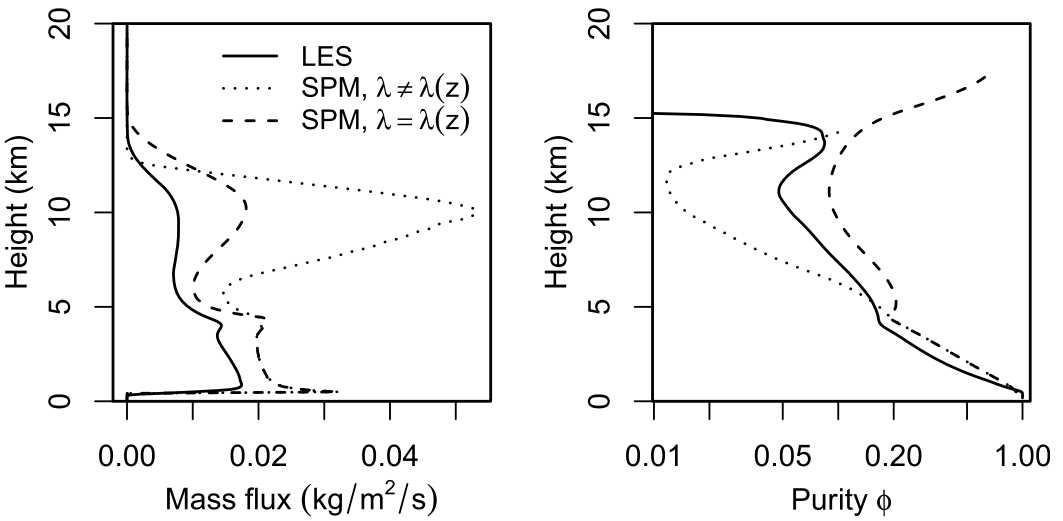

Figure 7. Profiles of (left) mass flux and (right) mass-flux-weighted in-cloud purity for (solid) the LES, (dotted) the SPM with the default parameters, which include $\lambda = 250$ m, and (dashed) the SPM modified to have $\lambda = 250$ m below the melting line and $\lambda = 1000$ m above the melting line. Note how using a larger λ above the melting line ameliorates both the upper-tropospheric biases in mass flux and purity.

humidity and ice concentration, and only a few will be listed here. One possible explanation is that SPAMIAC detrains its ice uniformly throughout the horizontal domain, while updrafts in the LES will tend to generate more concentrated patches of ice that will, due to a free-fall speed that depends on mass fraction, fall out faster. Another possibility is that SPAMIAC, by virtue of being a single-column model, lacks gravity waves that would dehydrate the upper troposphere. Finally, another possibility is that the current treatment of microphysics in the SPM is simply too crude to emulate some of the microphysical processes that are important for dehydrating the upper troposphere.

The last plot of Figure 6 shows the mass flux profiles for the LES and the SPM, calculated in the same way for both: counting only the mass flux of parcels with $w > 1$ m s^{-1} and $q_l + q_s > 10^{-5}$. As mentioned in section 6, the SPM mass flux is too large in the upper troposphere because the choice of $\lambda = 250$ m is too small there. Increasing λ in the upper troposphere simultaneously remedies the top-heaviness of the mass-flux profile and the spuriously low purity of upper-tropospheric updrafts. This is illustrated in Figure 7, which shows the RCE mass flux (left) and mass-flux-weighted purity (right) for the LES (solid), the ESPM with λ set to 250 m at all heights (dotted), and the ESPM with λ set to 250 m below the melting line and 1000 m above the melting line (dashed). Note how even this crude height dependence of λ greatly ameliorates the upper-tropospheric biases. For simplicity, however, and to avoid the slippery slope toward a major tuning exercise, only simulations with constant λ (and constant σ, SE, etc.) are shown henceforth.

To get an in-depth picture of how the LES and SPM updrafts compare, Figure 8 plots the normalized mass flux as a function of height (the ordinate) and various other updraft properties (the abscissa). To explain this in detail, consider the top-left plot, which has the liquid-water mass fraction q_l on the abscissa. At each height z, the colors indicate the distribution of normalized mass flux defined as

$$\frac{M(z, q_l)}{\max_{q_l'} M(z, q_l')}, \tag{22}$$

where $M(z, q_l)\Delta q_l$ is the mass flux of updrafts at height z with a liquid-water mass fraction between q_l and $q_l + \Delta q_l$. The mass flux distribution is normalized by its maximum at each height so that the distribution will be equally visible at all heights. There are six pairs of plots in Figure 8, which display the normalized mass flux as a function of liquid-water mass fraction, ice mass fraction, purity, equivalent potential temperature, buoyancy, and vertical velocity. Each pair is color coded and individual plots are labeled as either "LES" or "SPM."

Overall, Figure 8 demonstrates good agreement between the LES and the SPM. As noted in *Romps and Kuang* [2010b], the Lagrangian implementation of the SPM does a good job of replicating both the mean and variance of cloud properties in shallow convection. Here we see that this Eulerian implementation of the SPM is also able to replicate the mean and variance of cloud properties, in this case, for deep convection. Clearly, there is also room for improvement, and the application of more rigorous approaches to tuning and microphysics should realize some of that potential.

Although we will not attempt that tuning exercise here, Figure 9 gives a sense of the parameters to which the ESPM is most sensitive. The first seven plots correspond to the seven parameters in the current implementation of the ESPM. On the abscissa, one of those parameters varies over a plausible range while all other parameters are held fixed at their default values. In each plot, the root-mean-square error (RMSE) of mean ESPM profiles (relative to mean LES profiles) are plotted for six different observables: temperature T, relative humidity RH, cloud purity ϕ, cloud total water q_t, cloud buoyancy b, and cloud vertical velocity w. In these plots, lower values are better. For the environmental values T and RH, the RMSE is calculated from $z = 0$ to $z = 20$ km. For the cloud properties, the mean profiles are mass-flux-weighted and the RMSE is calculated from $z = 1$ km to $z = 10$ km.

It is clear from Figure 9 that the ESPM is most sensitive to independent variations in λ or σ. These variations alter the entrainment rate, which is equal to σ/λ. When λ and σ are both varied while holding σ/λ fixed (see the bottom-right plot), then the sensitivity is smaller. This is consistent with *Romps and Kuang* [2010b, Figure 7], which exhibited a valley of good λ and σ for the LSPM along a fixed value of σ/λ ($\sigma/\lambda = 3$ km^{-1} there for shallow convection, compared to $\sigma/\lambda = 1$ km^{-1} here for deep convection).

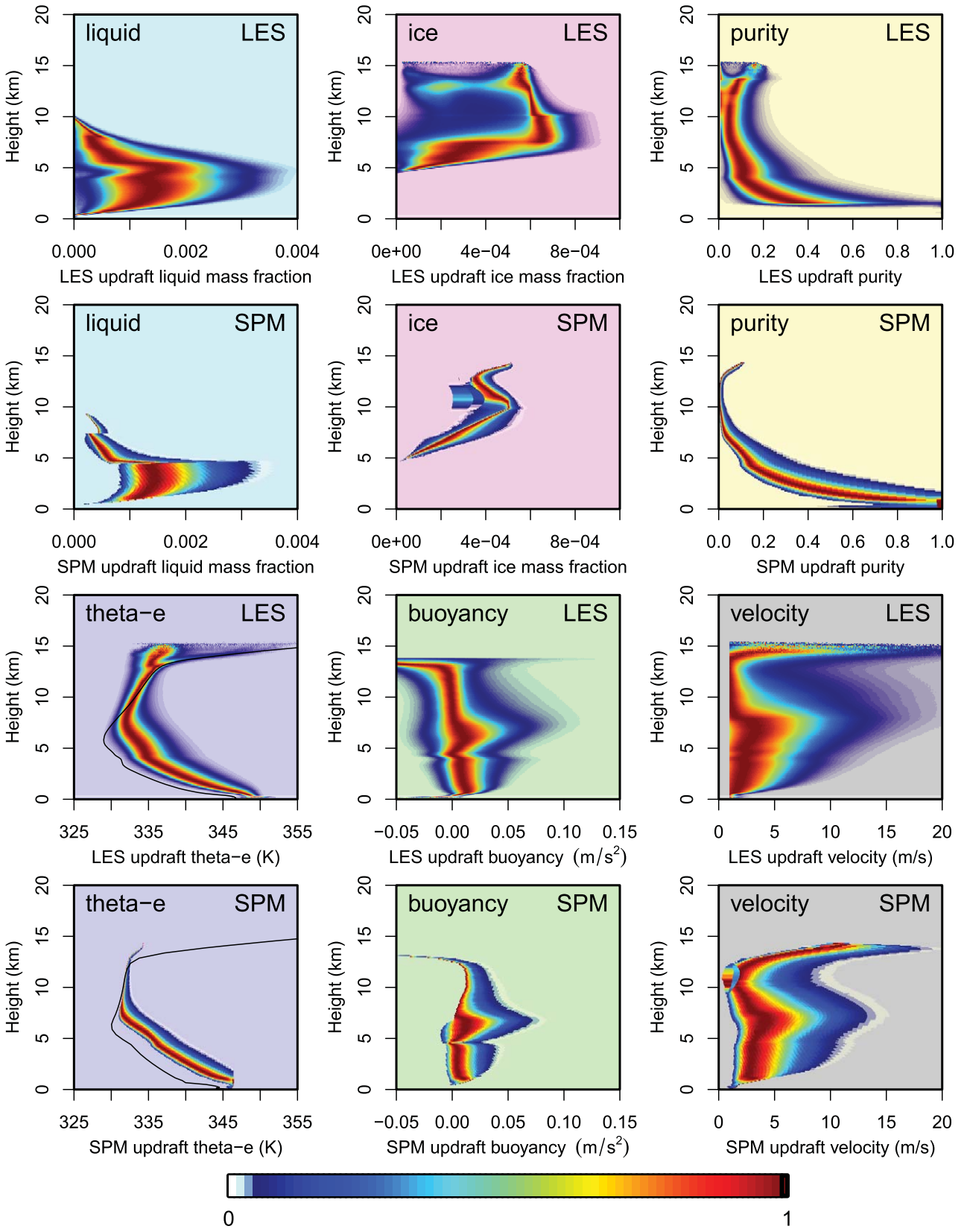

Figure 8. For the LES and SPM simulations, normalized mass-flux distributions as functions of various variables. See the text for details.

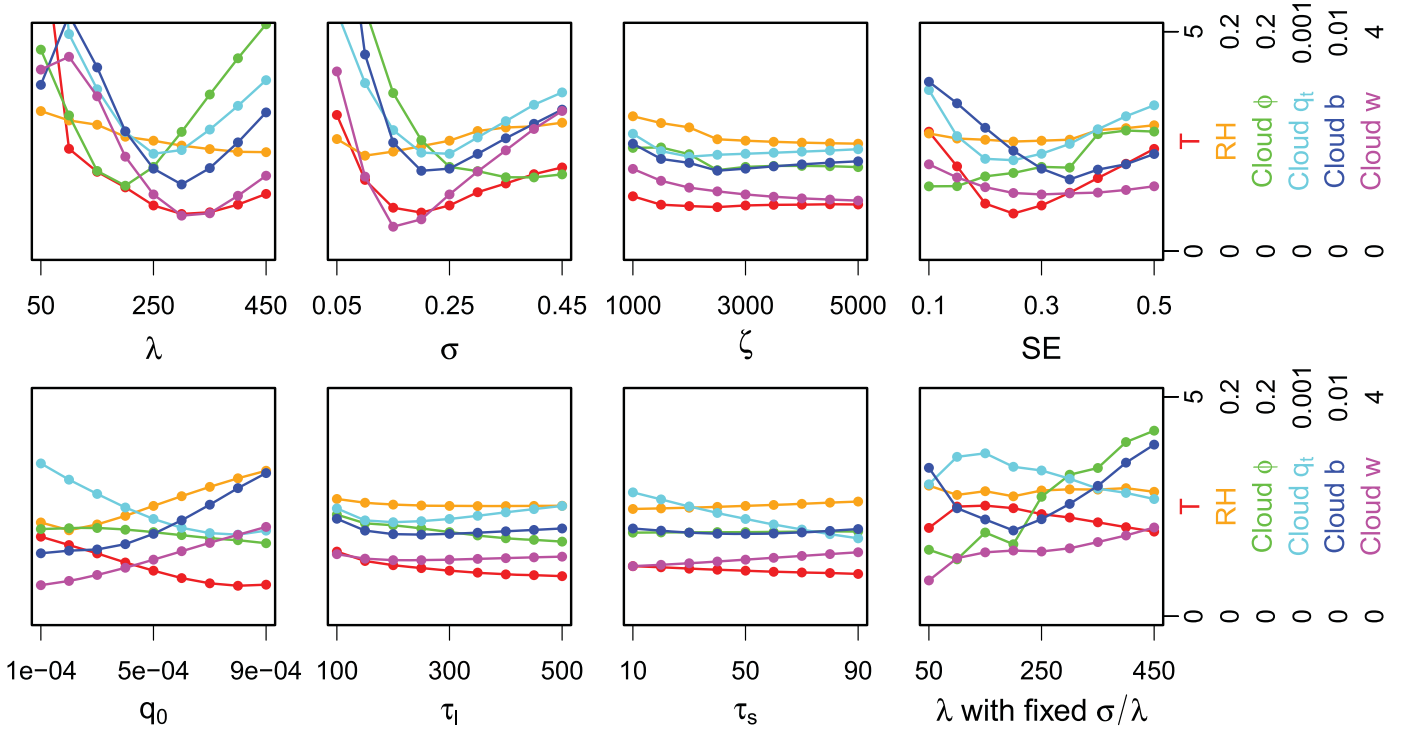

Figure 9. Height-weighted root-mean-square (RMS) errors between various LES and SPM mean profiles (environmental temperature T and relative humidity RH; mass-flux-weighted in-cloud purity ϕ, total water mass fraction q_t, buoyancy b, and vertical velocity w) for different values of SPM parameters (Poisson lengthscale λ, mean entrainment fraction σ, evaporation e-folding distance ζ, sedimentation efficiency SE, autoconversion threshold q_0, autoconversion time scale for liquid water τ_l, autoconversion time scale for solid water τ_s, and Poisson lengthscale λ with the entrainment rate σ/λ held fixed). All units are MKS: T (K), RH (dimensionless), ϕ (dimensionless), q_t (dimensionless), b (m s^{-2}), w (m s^{-1}), λ (m), σ (dimensionless), ζ (m), SE (dimensionless), q_0 (dimensionless), τ_l (s), and τ_s (s). Each circle corresponds to the RMS error calculated for the last 25 days of a 50 day SPM RCE simulation with the corresponding value of the parameter on the abscissa. Unless specified by the abscissa, parameters take their default values of $\lambda = 250$ m, $\sigma = 0.25$, $\zeta = 3$ km, SE=0.3, $q_0 = 5 \times 10^{-4}$, $\tau_l = 300$ s, and $\tau_s = 50$ s.

The next most influential parameters are the microphysical parameters of sedimentation efficiency SE and autoconversion threshold q_0. The ESPM is relatively insensitive to the microphysical parameters of evaporation e-folding distance ζ, liquid water autoconversion time scale τ_l, and solid water autoconversion time scale τ_s. Therefore, we can say that the ESPM has effectively only four degrees of parametric freedom: λ, σ, SE, and q_0.

9. Discussion

How does this Eulerian implementation of the Stochastic Parcel Model (ESPM) fit into the landscape of convective parameterizations? The most popular set of convective parameterizations are those that determine convective tendencies by first calculating convective mass fluxes. We may refer to these as mass-flux schemes. Within the set of mass-flux schemes are plume models and parcel models.

Plume models [e.g., *Arakawa and Schubert*, 1974; *Tiedtke*, 1989; *Kain and Fritsch*, 1990; *Zhang and McFarlane*, 1995] represent convection as either a single updraft (bulk plume) or a collection of updrafts (spectral plume). The obvious deficiency of bulk-plume models is that they are unable to represent the variance within cloudy updrafts. Spectral-plume models do have updraft variance, but the fact that each plume is distinguished by a constant entrainment rate produces updraft properties that are highly correlated in the vertical, while *Romps and Kuang* [2010b] showed in large-eddy simulations that stochastic entrainment dramatically reduces (or even virtually eliminates) those correlations. Parcel models [e.g., *Raymond and Blyth*, 1986; *Emanuel*, 1991; *Romps and Kuang*, 2010b; *Nie and Kuang*, 2012a; *Sušelj et al.*, 2013] represent convection as a collection of parcels, each of which are distinguished by the altitudes and intensities of their entrainment events. Before the advent of the ESPM, parcel models could be divided into two nonintersecting subsets, which we can refer to as type I and type II.

Type I parcel models produce deterministic convective tendencies, but have only a finite number of possible entrainment histories [*Raymond and Blyth*, 1986; *Emanuel*, 1991]. For example, in the scheme of *Raymond and Blyth* [1986], the cloud base mass flux is split into $9(N_z-1)$ parcels, where N_z is the number of vertical levels. Each parcel experiences exactly one entrainment event at one of the $N_z - 1$ levels above the lowest level, and environmental air is entrained there with one of nine possible entrainment fractions. Since the cloud base mass flux is apportioned into these $9(N_z - 1)$ parcels in fixed proportions, this scheme produces deterministic convective tendencies; in other words, given the same environmental conditions, the scheme is guaranteed to give the same result. On the other hand, the finite number of possible entrainment histories—i.e., only $9(N_z - 1)$, with only one entrainment event per parcel—greatly diminishes the physical realism of this approach.

Type II parcel models—i.e., the LSPM—have an infinite number of possible entrainment histories, but produce stochastic convective tendencies [*Romps and Kuang*, 2010b; *Nie and Kuang*, 2012a; *Sušelj et al*., 2013]. For each parcel of the LSPM, a Monte-Carlo method selects from an infinite number of possible entrainment histories, which correspond to the heights of the parcel's entrainment events and the amount of air entrained in each event. One of the key advantages of the LSPM is that its Poisson-process entrainment is motivated by and supported by LES results [*Romps and Kuang*, 2010b,a], while the treatment of entrainment in the existing type I schemes is contradicted by LES results [see *Romps and Kuang*, 2010a, Figure 6]. But, since only a finite number of parcels can be simulated in a Lagrangian fashion with a finite amount of computational effort, the LSPM's convective tendencies are necessarily stochastic. As discussed in the introduction, this source of noise is neither intentional nor desirable.

The ESPM is a new breed of parcel model that has the best features of both type I and type II schemes: it is deterministic like type I schemes and it gives parcels access to an infinite number of possible entrainment histories like type II schemes. This is accomplished by solving the $N=\infty$ LSPM under the approximation that there is no variance among parcels with the same height and purity. After some mathematical manipulation, the numerical implementation of the ESPM is described by equations (A5–A10) in Appendix A. These equations describe the integration of the ESPM as a sequence of matrix multiplications, which are amenable to efficient computation.

Finally, it is worth noting that the ESPM is highly configurable and extensible. Equations (A5–A10) may be thought of as a foundation upon which many variants of the ESPM may be built. The only assumption that is truly baked into those equations is the choice of an exponential distribution for the entrainment fraction, i.e., $f(\chi)=(1/\sigma)\exp(-\chi/\sigma)$. Everything else may be modified in a straightforward way. For example, if evidence warranted, the Poisson mixing length λ could be made a function of either height z or purity ϕ, or both. Or, since the results of *Nie and Kuang* [2012b] suggest that in-cloud mixing should cause parcels of the SPM to homogenize, a homogenization tendency could be added to the ESPM governing equations. Or, since recent work suggests that clouds feel aerodynamic drag [*Romps and Charn*, 2015; *Romps and Öktem*, 2015], a drag force could be added to the z-momentum source term S_w. Or, for example, the very simple microphysics described here could be replaced with a much more realistic microphysical scheme. With this large degree of configurability and extensibility, coupled with the best features of type I and type II parcel models, the ESPM is a promising foundation for future convective parameterizations.

Appendix A: Numerical Integration

Our goal here is to convert the SPM governing equation (5) to a matrix equation that can be solved numerically. First, we will discretize in height using a staggered grid. Let heights z_k, for integer k, be the interface heights at which the mass fluxes are defined. The scalar height in between z_k and z_{k+1}, which is the mean height at which mass is entrained and detrained as updrafts travel from z_k to z_{k+1}, will be denoted by $z_{k+1/2}$. For grid spacings that are much smaller than λ, the fraction of mass flux that experiences an entrainment event in between z_k and z_{k+1} is approximated well by $(z_{k+1}-z_k)/\lambda$. For the numerical implementation, a grid should always be chosen such that $z_{k+1}-z_k \ll \lambda$ for all k. But, to guarantee numerical stability even when this condition is violated, we will represent the fraction of mass flux that experiences an entrainment event in between z_k and z_{k+1} by $1-\exp[-(z_{k+1}-z_k)/\lambda]$. Note that this is the fraction of mass

flux that experiences one or more entrainment events; by using this discretization for $z_{k+1}-z_k \gtrsim \lambda$, the scheme will be numerically stable, but multiple entrainment events will be treated erroneously as single entrainment events. The cloud mass flux within $[\phi', \phi'+d\phi']$ at z_k that entrains between z_k and z_{k+1} is

$$d\phi'\, M(\phi', z_k)\left(1-e^{-(z_{k+1}-z_k)/\lambda}\right).$$

Therefore, equation (5) discretized in height becomes

$$\begin{aligned} M(\phi, z_{k+1})X(\phi, z_{k+1}) &= e^{-(z_{k+1}-z_k)/\lambda} M(\phi, z_k)X(\phi, z_k) \\ &+ (z_{k+1}-z_k)\frac{M(\phi, z_k)}{w(\phi, z_k)} S_X(\phi, z_k) - (z_{k+1}-z_k) d(\phi, z_k) X(\phi, z_k) \\ &+ \left[1-e^{-(z_{k+1}-z_k)/\lambda}\right] \int_0^1 d\phi'\, M(\phi', z_k)[X(\phi', z_k) + \chi X_e(z_k)] f(\chi) \left|\frac{\partial \chi}{\partial \phi}\right|. \end{aligned} \tag{A1}$$

Next, we will discretize ϕ by denoting the boundaries of bins by ϕ_i. We will approximate all variables as constant within a ϕ bin, and we will use index $i+\frac{1}{2}$ to denote values in the purity bin from ϕ_i to ϕ_{i+1}. Integrating over the ϕ bin ranging from ϕ_i to ϕ_{i+1}, we get

$$\begin{aligned} (\phi_{i+1}-\phi_i) M_{i+\frac{1}{2},k+1} X_{i+\frac{1}{2},k+1} &= (\phi_{i+1}-\phi_i) e^{-(z_{k+1}-z_k)/\lambda} M_{i+\frac{1}{2},k} X_{i+\frac{1}{2},k} \\ &+ (\phi_{i+1}-\phi_i)(z_{k+1}-z_k)\frac{M_{i+\frac{1}{2},k}}{w_{i+\frac{1}{2},k}} S_{X,i+\frac{1}{2},k} - (\phi_{i+1}-\phi_i)(z_{k+1}-z_k) d_{i+\frac{1}{2},k} X_{i+\frac{1}{2},k} \\ &+ \left[1-e^{-(z_{k+1}-z_k)/\lambda}\right] \int_0^1 d\phi' M(\phi', z_k) \int_{\phi_i}^{\phi_{i+1}} d\phi [X(\phi', z_k) + \chi X_e(z_k)] f(\chi) \left|\frac{\partial \chi}{\partial \phi}\right|. \end{aligned}$$

If there are N_ϕ purity bins with boundaries ranging from ϕ_1 to $\phi_{N_\phi+1}$, then this can be written as

$$\begin{aligned} (\phi_{i+1}-\phi_i) M_{i+\frac{1}{2},k+1} X_{i+\frac{1}{2},k+1} &= (\phi_{i+1}-\phi_i) e^{-(z_{k+1}-z_k)/\lambda} M_{i+\frac{1}{2},k} X_{i+\frac{1}{2},k} \\ &+ (\phi_{i+1}-\phi_i)(z_{k+1}-z_k)\frac{M_{i+\frac{1}{2},k}}{w_{i+\frac{1}{2},k}} S_{X,i+\frac{1}{2},k} - (\phi_{i+1}-\phi_i)(z_{k+1}-z_k) d_{i+\frac{1}{2},k} X_{i+\frac{1}{2},k} \\ &+ \left[1-e^{-(z_{k+1}-z_k)/\lambda}\right] \sum_{j=1}^{N_\phi} M_{j+\frac{1}{2},k} \int_{\phi_j}^{\phi_{j+1}} d\phi' \int_{\phi_i}^{\phi_{i+1}} d\phi [X_{j+\frac{1}{2},k} + \chi X_e(z_k)] f(\chi) \left|\frac{\partial \chi}{\partial \phi}\right|. \end{aligned} \tag{A2}$$

So long as the double integral can be solved, this is an expression for MX at z_{k+1} as a linear function of MX at z_k.

We will step through the evaluation of this double integral for $X = X_e = 1$ and then quote the result for general X and X_e. For $X = X_e = 1$, the double integral is

$$\int_{\phi_j}^{\phi_{j+1}} d\phi' \overbrace{\underbrace{\int_{\phi_i}^{\phi_{i+1}} d\phi \left|\frac{\partial \chi}{\partial \phi}\right| (1+\chi) f(\chi)}_{\star}}^{\dagger}.$$

Let us focus first on the inner integral, which we denote by a $\star$. Recall that $\chi = \phi'/\phi - 1$. Note that $\partial\chi/\partial\phi = -\phi'/\phi^2$, so a positive $d\phi$ corresponds to a negative $d\chi$. Therefore, in $\star$, we can write the integral over $d\phi$ times $|\partial\chi/\partial\phi|$ as the following integral over $d\chi$,

$$\int_{\phi_i}^{\phi_{i+1}} d\phi \left|\frac{\partial \chi}{\partial \phi}\right| = \int_{\chi(\phi_{i+1})}^{\chi(\phi_i)} d\chi\,,$$

where we are, for now, leaving the dependence of χ on ϕ' implicit. Using

$$f(\chi) = \frac{1}{\sigma}\mathcal{H}(\chi) e^{-\chi/\sigma}\,,$$

where $\mathcal{H}$ is the Heaviside step function, term $\star$ is

$$\star = [1+\sigma+\max[0,\chi(\phi_{i+1})]]\ e^{-\max[0,\chi(\phi_{i+1})]/\sigma} - [1+\sigma+\max[0,\chi(\phi_i)]]\ e^{-\max[0,\chi(\phi_i)]/\sigma}.$$

Since $\chi(\phi)=\phi'/\phi-1$, this can be written as

$$\star = \begin{cases} 0 & \phi' \le \phi_i \\ 1+\sigma-[1+\sigma+\chi(\phi_i)]e^{-\chi(\phi_i)/\sigma} & \phi_i < \phi' \le \phi_{i+1} \\ [1+\sigma+\chi(\phi_{i+1})]e^{-\chi(\phi_{i+1})/\sigma}-[1+\sigma+\chi(\phi_i)]e^{-\chi(\phi_i)/\sigma} & \phi_{i+1} < \phi' \end{cases}.$$

Integrating over $d\phi'$ from ϕ_j to ϕ_{j+1} to get term †, we find

$$\dagger = \int_{\phi_j}^{\phi_{j+1}} d\phi' \star \equiv F_{i,j} = \begin{cases} 0 & j < i \\ (1+\sigma)(\phi_{j+1}-\phi_j)-A_{i,j} & j=i \\ A_{i+1,j}-A_{i,j} & j > i \end{cases}, \tag{A3}$$

where

$$A_{i,j}=\sigma e^{1/\sigma}(\phi_j+2\sigma\phi_i)\ \exp\left(-\frac{\phi_j}{\phi_i\sigma}\right) - \sigma e^{1/\sigma}(\phi_{j+1}+2\sigma\phi_i)\ \exp\left(-\frac{\phi_{j+1}}{\phi_i\sigma}\right).$$

This gives an explicit and analytical expression for the double integral † in terms of σ and the boundaries of the ϕ bins.

For general X and X_e, the double integral becomes

$$\overbrace{\int_{\phi_j}^{\phi_{j+1}} d\phi' \underbrace{\int_{\phi_i}^{\phi_{i+1}} d\phi \left|\frac{\partial\chi}{\partial\phi}\right| [X_{j+\frac{1}{2},k}+\chi X_e(z_k)]f(\chi)}_{\star}}^{\dagger}.$$

In this case, we find

$$\dagger = \int_{\phi_j}^{\phi_{j+1}} d\phi' \star \equiv F^1_{i,j}X_{j+\frac{1}{2},k}+F^2_{i,j}X_e(z_k), \tag{A4}$$

where

$$F^{1,2}_{i,j} = \begin{cases} 0 & j < i \\ C^{1,2}_j-A^{1,2}_{i,j} & j=i \\ A^{1,2}_{i+1,j}-A^{1,2}_{i,j} & j > i \end{cases}, \tag{A5}$$

and

$$A^1_{i,j}=\sigma e^{1/\sigma}\phi_i\exp\left(-\frac{\phi_j}{\phi_i\sigma}\right) - \sigma e^{1/\sigma}\phi_i\exp\left(-\frac{\phi_{j+1}}{\phi_i\sigma}\right), \tag{A6}$$

$$C^1_j=\phi_{j+1}-\phi_j, \tag{A7}$$

$$A^2_{i,j}=\sigma e^{1/\sigma}(\phi_j+2\sigma\phi_i-\phi_i)\exp\left(-\frac{\phi_j}{\phi_i\sigma}\right) - \sigma e^{1/\sigma}(\phi_{j+1}+2\sigma\phi_i-\phi_i)\exp\left(-\frac{\phi_{j+1}}{\phi_i\sigma}\right), \tag{A8}$$

$$C^2_j=\sigma\phi_{j+1}-\phi_j. \tag{A9}$$

Then, governing equation (5) can be written as the following matrix equation,

$$
\begin{aligned}
(\phi_{i+1}-\phi_i)M_{i+\frac{1}{2},k+1}X_{i+\frac{1}{2},k+1} &= (\phi_{i+1}-\phi_i)e^{-(z_{k+1}-z_k)/\lambda}M_{i+\frac{1}{2},k}X_{i+\frac{1}{2},k} \\
+(\phi_{i+1}-\phi_i)(z_{k+1}-z_k)\frac{M_{i+\frac{1}{2},k}}{w_{i+\frac{1}{2},k}}S_{X,i+\frac{1}{2},k} &- (\phi_{i+1}-\phi_i)(z_{k+1}-z_k)d_{i+\frac{1}{2},k}X_{i+\frac{1}{2},k} \\
+\left[1-e^{-(z_{k+1}-z_k)/\lambda}\right]\sum_{j=1}^{N_\phi}M_{j+\frac{1}{2},k}&\left[F^1_{i,j}X_{j+\frac{1}{2},k}+F^2_{i,j}X_e(z_k)\right].
\end{aligned}
\tag{A10}
$$

This equation reduces the calculation of SPM fluxes to a sequence of matrix additions and multiplications. Note that the matrices $F^1_{i,j}$ and $F^2_{i,j}$ are functions only of σ and the ϕ-bin boundaries, so they can be precomputed and saved in a lookup table.

Appendix B: Precipitation Fluxes

Once water has undergone autoconversion, it takes on the same temperature and horizontal velocity as the environment and it contributes to the free-fall mass fluxes $\tilde{F}_{l,\mathrm{ff}}$ and $\tilde{F}_{s,\mathrm{ff}}$. Here and in the remaining appendices, we denote by a tilde a quantity that is a function of z only (i.e., already integrated over ϕ). The subscript l refers to liquid water, the subscript s refers to solid water, and the subscript ff refers to free fall. We can define $\widetilde{\mathrm{Auto}}_l$ and $\widetilde{\mathrm{Auto}}_s$ as the total rates of autoconversion in units of kg m^{-3} s^{-1}, which are related to the Auto_l and Auto_s of equations (7) and (8) by

$$
\widetilde{\mathrm{Auto}}_l(z)=\int_0^1 d\phi\,\frac{M(\phi,z)}{w(\phi,z)}\mathrm{Auto}_l(\phi,z), \tag{B1}
$$

$$
\widetilde{\mathrm{Auto}}_s(z)=\int_0^1 d\phi\,\frac{M(\phi,z)}{w(\phi,z)}\mathrm{Auto}_s(\phi,z)\,. \tag{B2}
$$

Let us define the sedimentation efficiency SE as the fraction of precipitating water that falls to the surface without evaporating or sublimating. Let us assume that the profile of evaporation and sublimation of precipitation formed at z has an exponential shape that decays downward from z with an e-folding distance ζ, which is a tunable parameter. Then, the contribution to $\tilde{F}_{l,\mathrm{ff}}(z)$ from $\widetilde{\mathrm{Auto}}_l$ in between z' and $z'+dz'$ is

$$
-\widetilde{\mathrm{Auto}}_l(z')\,dz'\,\mathcal{H}(z'-z)\left\{\mathrm{SE}+(1-\mathrm{SE})\frac{e^{z/\zeta}-e^{z_s/\zeta}}{e^{z'/\zeta}-e^{z_s/\zeta}}\right\},
$$

where $\mathcal{H}$ is the Heaviside unit step function. Note that the minus sign is here because $\tilde{F}_{l,\mathrm{ff}}$ is a downward pointing flux. The contribution to $\tilde{F}_{l,\mathrm{ff}}(z)$ from $\widetilde{\mathrm{Auto}}_s$ in between z' and $z'+dz'$ is

$$
-\widetilde{\mathrm{Auto}}_s(z')\,dz'\,\mathcal{H}(z'-z)\mathcal{H}\left[T_e(z)-T_{\mathrm{trip}}\right]\left\{\mathrm{SE}+(1-\mathrm{SE})\frac{e^{z/\zeta}-e^{z_s/\zeta}}{e^{z'/\zeta}-e^{z_s/\zeta}}\right\},
$$

while its contribution to $\tilde{F}_{s,\mathrm{ff}}(z)$ is

$$
-\widetilde{\mathrm{Auto}}_s(z')\,dz'\,\mathcal{H}(z'-z)\mathcal{H}\left[T_{\mathrm{trip}}-T_e(z)\right]\left\{\mathrm{SE}+(1-\mathrm{SE})\frac{e^{z/\zeta}-e^{z_s/\zeta}}{e^{z'/\zeta}-e^{z_s/\zeta}}\right\}.
$$

Therefore,

$$
\begin{aligned}
\tilde{F}_{l,\mathrm{ff}}(z) = &-\int_z^\infty dz'\,\widetilde{\mathrm{Auto}}_l(z')\left\{\mathrm{SE}+(1-\mathrm{SE})\frac{e^{z/\zeta}-e^{z_s/\zeta}}{e^{z'/\zeta}-e^{z_s/\zeta}}\right\} \\
&-\mathcal{H}\left[T_e(z)-T_{\mathrm{trip}}\right]\int_z^\infty dz'\,\widetilde{\mathrm{Auto}}_s(z')\left\{\mathrm{SE}+(1-\mathrm{SE})\frac{e^{z/\zeta}-e^{z_s/\zeta}}{e^{z'/\zeta}-e^{z_s/\zeta}}\right\},
\end{aligned}
\tag{B3}
$$

$$
\tilde{F}_{s,\mathrm{ff}}(z) = -\mathcal{H}\left[T_{\mathrm{trip}}-T_e(z)\right]\int_z^\infty dz'\,\widetilde{\mathrm{Auto}}_s(z')\left\{\mathrm{SE}+(1-\mathrm{SE})\frac{e^{z/\zeta}-e^{z_s/\zeta}}{e^{z'/\zeta}-e^{z_s/\zeta}}\right\}. \tag{B4}
$$

Appendix C: Net Fluxes and Sources

The SPM must feed to its host model the fluxes of mass, total enthalpy, momentum, vapor, liquid, and solid, as well as the sources of these quantities within updrafts (which are zero except for vapor, liquid, and solid). The updraft plus free-fall fluxes of these quantities are calculated as follows:

$$\tilde{F}_{\text{mass}}(z)=\int_0^1 d\phi\, M(\phi,z)+\tilde{F}_{l,\text{ff}}(z)+\tilde{F}_{s,\text{ff}}(z), \tag{C1}$$

$$\tilde{F}_{\text{enth}}(z)=\int_0^1 d\phi\, M(\phi,z)H_{\text{tot}}(\phi,z)+\tilde{F}_{l,\text{ff}}(z)H_{\text{tot},l,e}(z)+\tilde{F}_{\text{ff},s}(z)H_{\text{tot},s,e}(z), \tag{C2}$$

$$\vec{\tilde{F}}_{\text{mom}}(z)=\int_0^1 d\phi\, M(\phi,z)\vec{u}(\phi,z)+\left[\tilde{F}_{l,\text{ff}}(z)+\tilde{F}_{s,\text{ff}}(z)\right]\vec{u}_e, \tag{C3}$$

$$\tilde{F}_v(z)=\int_0^1 d\phi\, M(\phi,z)q_v(\phi,z), \tag{C4}$$

$$\tilde{F}_l(z)=\int_0^1 d\phi\, M(\phi,z)q_l(\phi,z)+\tilde{F}_{\text{ff},l}(z), \tag{C5}$$

$$\tilde{F}_s(z)=\int_0^1 d\phi\, M(\phi,z)q_s(\phi,z)+\tilde{F}_{s,\text{ff}}(z)\,, \tag{C6}$$

where $H_{\text{tot}}(\phi,z)=h(\phi,z)+|\vec{u}(\phi,z)|^2/2$ and h is the MSE. The values $H_{\text{tot},l,e}(z)$ and $H_{\text{tot},s,e}(z)$ are the MSE of liquid and solid water at the environmental temperature $T_e(z)$ plus the specific kinetic energy of the environment $|\vec{u}_e(z)|^2/2$.

The sources of vapor, liquid, and solid are given in terms of Evap and Melt, which we recall are the per-ϕ-bin rates in updrafts only (i.e., they do not include any evaporation or melting that may occur in the GCM once liquid or solid is detrained by convection or deposited by the convergence of a free-fall flux). In particular,

$$\tilde{S}_v=\int_0^1 d\phi\,\frac{M(\phi,z)}{w(\phi,z)}\,\text{Evap}(\phi,z), \tag{C7}$$

$$\tilde{S}_l=\int_0^1 d\phi\,\frac{M(\phi,z)}{w(\phi,z)}\,[\text{Melt}(\phi,z)-\text{Evap}(\phi,z)], \tag{C8}$$

$$\tilde{S}_s=-\int_0^1 d\phi\,\frac{M(\phi,z)}{w(\phi,z)}\,\text{Melt}(\phi,z)\,. \tag{C9}$$

Appendix D: Positive-Definite Treatment of Water

The fluxes of water calculated by the SPM could lead to negative water densities over the time step used by the host model if those fluxes are not appropriately limited. For vapor, liquid, and solid, we cannot apply a positive-definite flux limiter to each separately because there are sources and sinks of each, and the sources and sinks move mass between those three categories at each height. Instead, we will need to proceed in a multistep fashion. Let us define $\vec{F}$ as a height-dependent three-vector with components $\tilde{F}_v$, $\tilde{F}_l$, and $\tilde{F}_s$. We then decompose $\vec{F}$ into two vectors: $\vec{F}_{1\text{way}}$, in which all of the components are of the same sign, and $\vec{F}_{2\text{way}}$, whose components sum to zero. We define the components of $\vec{F}_{2\text{way}}$ as

$$F_{2\text{way},i}=\begin{cases}0 & \sum_j |F_j|=0\\ \frac{1}{2}\left[F_i-s|F_i|-(F_i+s|F_i|)\dfrac{\sum_j\left(F_j-s|F_j|\right)}{\sum_k\left(F_k+s|F_k|\right)}\right] & \text{otherwise}\end{cases},$$

where

$$s = \begin{cases} 1 & \sum_i F_i \geq 0 \\ -1 & \sum_i F_i < 0 \end{cases},$$

and $\vec{F}_{1\text{way}} \equiv \vec{F} - \vec{F}_{2\text{way}}$. Defining

$$\tilde{F} = \sum_{i=1}^{3} F_{1\text{way},i}$$

as the net water flux, we apply a one-dimensional positive-definite flux limiter to $\tilde{F}$ to ensure that the total water mass does not go negative. This flux limiter is described in Appendix E.

Let us denote by $\tilde{F}^{\text{pos}}$ the flux-limited water flux. We then define a flux-limited version of $\vec{F}_{1\text{way}}$ as

$$\vec{F}^{\text{pos}}_{1\text{way}} = \frac{\tilde{F}^{\text{pos}}}{\tilde{F}} \vec{F}_{1\text{way}}, \tag{D1}$$

and then the flux-limited version of $\vec{F}$ is

$$\vec{F}^{\text{pos}} = \vec{F}^{\text{pos}}_{1\text{way}} + \vec{F}_{2\text{way}}. \tag{D2}$$

The components of this vector are the corrected component-wise fluxes $\tilde{F}^{\text{pos}}_v$, $\tilde{F}^{\text{pos}}_l$, and $\tilde{F}^{\text{pos}}_s$. We then apply these corrected fluxes, as well as the uncorrected rates of evaporation and melting, to the host model over its time step. This will guarantee nonnegative total water at each level, but will not guarantee that vapor, liquid, or solid are separately nonnegative. To regain nonnegative water classes, we move mass among the water classes at each level to bring the negative values up to zero. In particular, defining $\vec{q}$ with the three components q_v, q_l, and q_s, we then calculate a corrected vector $\vec{q}^{\text{pos}}$, with components defined as

$$q^{\text{pos}}_i = \begin{cases} 0 & \sum_j |q_j| = 0 \\ (q_i + |q_i|) \dfrac{\sum_j q_j}{\sum_k (q_k + |q_k|)} & \text{otherwise} \end{cases}. \tag{D3}$$

The movement of mass generated by this algorithm is then recorded as an appropriate amount of additional evaporation and sublimation, which are added to $\tilde{S}_v$, $\tilde{S}_l$, and $\tilde{S}_s$ to produce the corrected sources $\tilde{S}^{\text{pos}}_v$, $\tilde{S}^{\text{pos}}_l$, and $\tilde{S}^{\text{pos}}_s$.

Appendix E: One-Dimensional Flux Limiter

We describe here a simple and minimally invasive positive-definite flux limiter for fluxes on a one-dimensional line segment. The advantages of this flux limiter over other flux limiters are (1) that it uses nonlocal information to impose minimally invasive limits (which is possible due to the one-dimensional nature of the grid), and (2) that it works just as well for very large CFL numbers. Although this scheme is developed with a GCM grid column in mind, it is equally applicable to fluxes on any line segment. The idea behind the scheme is that each grid box k has its outgoing fluxes scaled down by a common factor of α^k, where $0 \leq \alpha^k \leq 1$. To be minimally invasive, we wish to find the set of α^k that are all as close as possible to one.

To accomplish this, we first find all of the grid cells that have no incoming fluxes from another grid cell; let NI (for "no incoming") be the set of those grid cells. A cell at the end of the line segment is considered a member of NI if it has no incoming flux from its one neighbor, regardless of the flux going into or out of that end of the line segment. Next, we find all of the grid cells that have no outgoing fluxes to another grid cell; let NO (for "no outgoing") be the set of those grid cells. A cell at the end of the line segment is considered a member of NO if it has no outgoing flux to its one neighbor, regardless of the flux going into or out of that end of the line segment. Once the sets NI and NO have been identified, the assignment of the flux limiters starts with the grid cells in NI. Since each NI grid cell has no unknown fluxes coming in

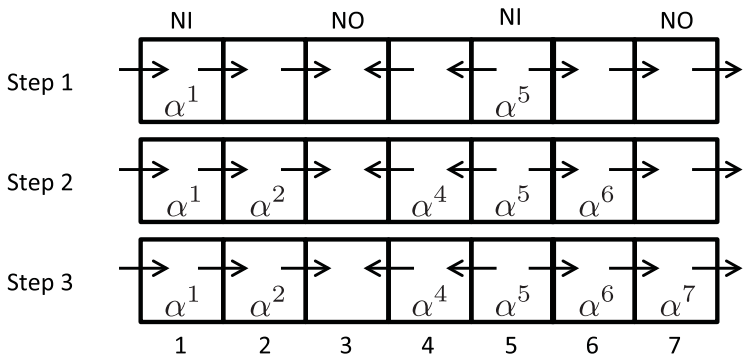

Figure 10. An example of assigning flux limiters to a line segment with seven grid cells. The arrows show the direction of the fluxes at the interfaces. In this case, there are two NI grid cells and two NO grid cells. Marching outward from the NI grid cells, it takes three steps to find the minimally invasive flux limiters for this case.

(for an NI grid cell on an end, we know exactly what the incoming fluxes are), we can immediately define α^k for each NI grid cell as

$$\alpha^k = \min\left[1, \frac{\Delta z^k \rho^k + \Delta t\, \tilde{F}^{\text{in},\alpha}}{\Delta t\, \tilde{F}^{\text{out}}}\right], \tag{E1}$$

where ρ^k is the density in grid k, Δz^k is the grid spacing, Δt is the time step, $\tilde{F}^{\text{out}}$ is the sum of the magnitudes of all the outgoing fluxes, and $\tilde{F}^{\text{in},\alpha}$ is the sum of the magnitudes of all the incoming fluxes reduced by their origin grid cell's α factor (for NI, incoming fluxes are possibly nonzero only for an end grid cell, and fluxes into the line segment have $\alpha = 1$ since the requirement of positive-definite masses places no restrictions on them). Any flux outgoing from a grid cell k in NI is now reduced in magnitude by α^k.

We then assign the flux limiters iteratively to the remaining grid cells using equation (E1), marching outward from NI grid cells until we end in NO grid cells. For example, in step 2, we go to every non-NI grid cell that is adjacent to an NI grid cell. If the grid cell is an NO grid cell, then there is nothing to do (i.e., no need to assign a flux limiter when there are no outgoing fluxes) unless the cell is on an end with a flux going to outside the line segment; in that case, we can calculate its α factor using equation (E1). Otherwise, if the grid cell is not in NO, then we already know all of the α factors needed to calculate the grid cell's $\tilde{F}^{\text{in},\alpha}$ and, therefore, to calculate its α factor using equation (E1). Proceeding in this way from NI cells to NO cells, we find the minimally invasive set of flux limiters.

Figure 10 illustrates this procedure for a line segment with seven grid cells. In this case, there are two NI grid cells and two NO grid cells. Note that end grid cells are always either NI or NO. If both are NO, then there must be an NI grid cell in the interior. Either way, there is always at least one NI grid cell. In step 1, the α factors are calculated according to equation (E1) for the NI grid cells. In step 2, the α factors are calculated according to equation (E1) for the cells adjacent to NI grid cells. In step 3, which happens to be the final step for this case, the flux limiter for grid 7 is defined. Note that flux limiters are not needed for interior NO cells since they have no outgoing fluxes and, therefore, there is nothing to be limited.

Appendix F: Host-Model Tendencies

The tendencies of per-volume host-model mass, energy, momentum, vapor, liquid, and solid are $-\partial\tilde{F}_{\text{mass}}/\partial z$, $-\partial\tilde{F}_{\text{enth}}/\partial z$, $-\partial\vec{\tilde{F}}_{\text{mom}}/\partial z$, $\tilde{S}_v^{\text{pos}} - \partial\tilde{F}_v^{\text{pos}}/\partial z$, $\tilde{S}_l^{\text{pos}} - \partial\tilde{F}_l^{\text{pos}}/\partial z$, and $\tilde{S}_s^{\text{pos}} - \partial\tilde{F}_s^{\text{pos}}/\partial z$, respectively. Since the SPM grid is chosen so that the host-model interfaces coincide with SPM interfaces, the fluxes are naturally defined on host-model interfaces and the sources are naturally defined on the volumes in between. This makes it straightforward to calculate tendencies for host-model grid boxes. In addition to the updraft and free-fall fluxes, we impose compensating mass fluxes equal to $-\int_0^1 d\phi\, M(\phi, z)$ that carry the environmental properties. Like the convective and free-fall fluxes, these are defined on host-model interfaces. The environmental properties on those interfaces are calculated using third-order upwind interpolation and limited, as need, with the Thuburn flux limiter [*Thuburn*, 1996].

Appendix G: Fractional Entrainment Rate

We can calculate the fractional entrainment rate by integrating equation (3), which gives the change in M due to entrainment only. Integrating over ϕ gives

$$\left(\frac{\partial}{\partial z}\int_0^1 d\phi\, M(\phi,z)\right)_{\text{entrainment}} =$$
$$-\int_0^1 d\phi\,\frac{M(\phi,z)}{\lambda}+\int_0^1 d\phi'\,\frac{M(\phi',z)}{\lambda}\int_0^\infty d\chi\, f(\chi)+\int_0^1 d\phi'\,\frac{M(\phi',z)}{\lambda}\int_0^\infty d\chi\,\chi f(\chi)\,.$$

Since the integral of $f(\chi)$ over χ gives one, the first two terms on the right-hand side cancel. Therefore, we find that

$$\left(\frac{\partial}{\partial z}\int_0^1 d\phi\, M(\phi,z)\right)_{\text{entrainment}} = \int_0^1 d\phi\, M(\phi,z)\frac{\sigma}{\lambda}\,,$$

where $\sigma=\int d\chi\,\chi f(\chi)$ is the mean χ for entrainment events. In other words, $(\partial\tilde{M}/\partial z)_{\text{entrainment}}=\varepsilon\tilde{M}$, where $\varepsilon=\sigma/\lambda$ is the fractional entrainment rate.

Acknowledgments
This work was supported by the Scientific Discovery through Advanced Computing (SciDAC) program funded by the U.S. Department of Energy Office of Advanced Scientific Computing Research and Office of Biological and Environmental Research under contract DE-AC02-05CH11231. We note that there are no data sharing issues since all of the numerical information is provided in the figures.

References

Arakawa, A., and W. Schubert (1974), Interaction of a cumulus cloud ensemble with the large-scale environment, Part I, *J. Atmos. Sci.*, *31*(31), 674–701.
Böing, S. J., H. J. J. Jonker, A. P. Siebesma, and W. W. Grabowski (2012), Influence of the subcloud layer on the development of a deep convective ensemble, *J. Atmos. Sci.*, *69*(9), 2682–2698.
Böing, S. J., H. J. J. Jonker, W. A. Nawara, and A. P. Siebesma (2014), On the deceiving aspects of mixing diagrams of deep cumulus convection, *J. Atmos. Sci.*, *71*(1), 56–68.
Chikira, M. (2010), A cumulus parameterization with state-dependent entrainment rate. Part II: Impact on climatology in a general circulation model, *J. Atmos. Sci.*, *67*(7), 2194–2211.
Clough, S. A., M. W. Shephard, E. J. Mlawer, J. S. Delamere, M. J. Iacono, K. Cady-Pereira, S. Boukabara, and P. D. Brown (2005), Atmospheric radiative transfer modeling: A summary of the AER codes, *J. Quant. Spectrosc. Radiat. Transfer*, *91*(2), 233–244.
Davies, L., C. Jakob, P. May, V. V. Kumar, and S. Xie (2013), Relationships between the large-scale atmosphere and the small-scale convective state for Darwin, Australia, *J. Geophys. Res. Atmos.*, *118*, 11,534–11,545, doi:10.1002/jgrd.50645.
Dawe, J. T., and P. H. Austin (2011), Interpolation of LES cloud surfaces for use in direct calculations of entrainment and detrainment, *Mon. Weather Rev.*, *139*(2), 444–456.
Emanuel, K. A. (1991), A scheme for representing cumulus convection in large-scale models, *J. Atmos. Sci.*, *48*(21), 2313–2329.
Fierro, A. O., J. M. Simpson, M. A. Lemone, J. M. Straka, and B. F. Smull (2009), On how hot towers fuel the Hadley cell: An observational and modeling study of line-organized convection in the equatorial trough from TOGA COARE, *J. Atmos. Sci.*, *66*(9), 2730–2746.
Gregory, D., and P. R. Rowntree (1990), A mass flux convection scheme with representation of cloud ensemble characteristics and stability-dependent closure, *Mon. Weather Rev.*, *118*(7), 1483–1506.
Held, I. M., M. Zhao, and B. Wyman (2007), Dynamic radiative-convective equilibria using GCM column physics, *J. Atmos. Sci.*, *64*(1), 228–238.
Heus, T., G. van Dijk, H. Jonker, and H. Van den Akker (2008), Mixing in shallow cumulus clouds studied by Lagrangian particle tracking, *J. Atmos. Sci.*, *65*(8), 2581–2597.
Hirota, N., Y. N. Takayabu, M. Watanabe, M. Kimoto, and M. Chikira (2014), Role of convective entrainment in spatial distributions of and temporal variations in precipitation over tropical oceans, *J. Clim.*, *27*(23), 8707–8723.
Iacono, M. J., J. S. Delamere, E. J. Mlawer, M. W. Shephard, S. A. Clough, and W. D. Collins (2008), Radiative forcing by long-lived greenhouse gases: Calculations with the AER radiative transfer models, *J. Geophys. Res.*, *113*, D13103, doi:10.1029/2008JD009944.
Jakob, C., and A. P. Siebesma (2003), A new subcloud model for mass-flux convection schemes: Influence on triggering, updraft properties, and model climate, *Mon. Weather Rev.*, *131*(11), 2765–2778.
Jeevanjee, N., and D. M. Romps (2013), Convective self-aggregation, cold pools, and domain size, *Geophys. Res. Lett.*, *40*, 1–5, doi:10.1002/grl.50204.
Jeevanjee, N., and D. M. Romps (2015), Effective buoyancy, inertial pressure, and the mechanical generation of boundary-layer mass flux by cold pools, *J. Atmos. Sci.*, *72*(8), 3199–3213.
Kain, J. S., and J. M. Fritsch (1990), A one-dimensional entraining/detraining plume model and its application in convective parameterization, *J. Atmos. Sci.*, *47*(23), 2784–2802.
Khairoutdinov, M., and D. Randall (2006), High-resolution simulation of shallow-to-deep convection transition over land, *J. Atmos. Sci.*, *63*(12), 3421–3436.
Klocke, D., R. Pincus, and J. Quaas (2011), On constraining estimates of climate sensitivity with present-day observations through model weighting, *J. Clim.*, *24*(23), 6092–6099.
Knight, C. G., et al. (2007), Association of parameter, software, and hardware variation with large-scale behavior across 57,000 climate models, *Proc. Natl. Acad. Sci. U. S. A.*, *104*(30), 12,259–12,264.
Kuang, Z., and C. S. Bretherton (2006), A mass-flux scheme view of a high-resolution simulation of a transition from shallow to deep cumulus convection, *J. Atmos. Sci.*, *63*(7), 1895–1909.
Lawrence, M. G., and P. J. Rasch (2005), Tracer transport in deep convective updrafts: Plume ensemble versus bulk formulations, *J. Atmos. Sci.*, *62*(8), 2880–2894.
Lin, C., and A. Arakawa (1997), The macroscopic entrainment processes of simulated cumulus ensemble. Part I: Entrainment sources, *J. Atmos. Sci.*, *54*(8), 1027–1043.
Lin, J.-L., T. Qian, T. Shinoda, and S. Li (2015), Is the tropical atmosphere in convective quasi-equilibrium?, *J. Clim.*, *28*(11), 4357–4372.
Mapes, B., and R. Houze (1992), An integrated view of the 1987 Australian monsoon and its mesoscale convective systems. I: Horizontal structure, *Q. J. R. Meteorol. Soc.*, *118*(507), 927–963.
McBride, J. L., and W. M. Frank (1999), Relationships between stability and monsoon convection, *J. Atmos. Sci.*, *56*(1), 24–36.
Moorthi, S., and M. J. Suarez (1992), Relaxed Arakawa-Schubert. A parameterization of moist convection for general circulation models, *Mon. Weather Rev.*, *120*(6), 978–1002.

Nie, J., and Z. Kuang (2012a), Responses of shallow cumulus convection to large-scale temperature and moisture perturbations: A comparison of large-eddy simulations and a convective parameterization based on stochastically entraining parcels, *J. Atmos. Sci.*, *69*(6), 1936–1956.

Nie, J., and Z. Kuang (2012b), Beyond bulk entrainment and detrainment rates: A new framework for diagnosing mixing in cumulus convection, *Geophys. Res. Lett.*, *39*, L21803, doi:10.1029/2012GL053992.

Raymond, D. J., and A. M. Blyth (1986), A stochastic model for non-precipitating convection, *J. Atmos. Sci.*, *43*, 2708–2718.

Romps, D. M. (2008), The dry-entropy budget of a moist atmosphere, *J. Atmos. Sci.*, *65*(12), 3779–3799.

Romps, D. M. (2010), A direct measure of entrainment, *J. Atmos. Sci.*, *67*(6), 1908–1927.

Romps, D. M. (2015), MSE minus CAPE is the true conserved variable for an adiabatically lifted parcel, *J. Atmos. Sci.*, *72*(9), 3639–3646.

Romps, D. M., and A. B. Charn (2015), Sticky thermals: Evidence for a dominant balance between buoyancy and drag in cloud updrafts, *J. Atmos. Sci.*, *72*(8), 2890–2901.

Romps, D. M., and Z. Kuang (2010a), Do undiluted convective plumes exist in the upper tropical troposphere?, *J. Atmos. Sci.*, *67*(2), 468–484.

Romps, D. M., and Z. Kuang (2010b), Nature versus nurture in shallow convection, *J. Atmos. Sci.*, *67*(5), 1655–1666.

Romps, D. M., and R. Öktem (2015), Stereo photogrammetry reveals substantial drag on cloud thermals, *Geophys. Res. Lett.*, *42*(12), 5051–5057.

Rougier, J., D. M. H. Sexton, J. M. Murphy, and D. Stainforth (2009), Analyzing the climate sensitivity of the HadSM3 climate model using ensembles from different but related experiments, *J. Clim.*, *22*(13), 3540–3557.

Sanderson, B., C. Piani, W. Ingram, D. Stone, and M. Allen (2008), Towards constraining climate sensitivity by linear analysis of feedback patterns in thousands of perturbed-physics GCM simulations, *Clim. Dyn.*, *30*(2), 175–190.

Siebesma, A. P., and A. A. M. Holtslag (1996), Model impacts of entrainment and detrainment rates in shallow cumulus convection, *J. Atmos. Sci.*, *53*(16), 2354–2364.

Sušelj, K., J. Teixeira, and D. Chung (2013), A unified model for moist convective boundary layers based on a stochastic eddy-diffusivity/mass-flux parameterization, *J. Atmos. Sci.*, *70*(7), 1929–1953.

Taylor, G. R., and M. B. Baker (1991), Entrainment and detrainment in cumulus clouds, *J. Atmos. Sci.*, *48*, 112–121.

Telford, J. W. (1975), Turbulence, entrainment, and mixing in cloud dynamics, *Pure Appl. Geophys.*, *113*(1), 1067–1084.

Thayer-Calder, K., and D. Randall (2015), A numerical investigation of boundary layer quasi-equilibrium, *Geophys. Res. Lett.*, *42*,550–556, doi:10.1002/2014GL062649.

Thompson, R. M., S. W. Payne, E. E. Recker, and R. J. Reed (1979), Structure and properties of synoptic-scale wave disturbances in the Intertropical Convergence Zone of the Eastern Atlantic, *J. Atmos. Sci.*, *36*(1), 53–72.

Thuburn, J. (1996), Multidimensional flux-limited advection schemes, *J. Comput. Phys.*, *123*(1), 74–83.

Tiedtke, M. (1989), A comprehensive mass flux scheme for cumulus parameterization in large-scale models, *Mon. Weather Rev.*, *117*(8), 1779–1800.

Tokioka, T., K. Yamazaki, A. Kitoh, and T. Ose (1988), The equatorial 30-60 day oscillation and the Arakawa-Schubert penetrative cumulus parameterization, *J. Meteorol. Soc. Jpn.*, *66*(6), 883–901.

Tompkins, A. M. (2001), Organization of tropical convection in low vertical wind shears: The role of cold pools, *J. Atmos. Sci.*, *58*(13), 1650–1672.

Torri, G., Z. Kuang, and Y. Tian (2015), Mechanisms for convection triggering by cold pools, *Geophys. Res. Lett.*, *42*, 1943–1950, doi:10.1002/2015GL063227.

Watanabe, M., M. Chikira, Y. Imada, and M. Kimoto (2011), Convective control of ENSO simulated in MIROC, *J. Clim.*, *24*, 543–562.

Yano, J.-I., M. Bister, V. Fuchs, L. Gerard, V. T. J. Phillips, S. Barkidija, and J.-M. Piriou (2013), Phenomenology of convection-parameterization closure, *Atmos. Chem. Phys.*, *13*(8), 4111–4131.

Yeo, K., and D. M. Romps (2013), Measurement of convective entrainment using Lagrangian particles, *J. Atmos. Sci.*, *70*(1), 266–277.

Zhang, G. J., and N. A. McFarlane (1995), Sensitivity of climate simulations to the parameterization of cumulus convection in the Canadian Climate Centre general circulation model, *Atmos. Ocean*, *33*(3), 407–446.

Zuidema, P., Z. Li, R. J. Hill, L. Bariteau, B. Rilling, C. Fairall, W. A. Brewer, B. Albrecht, and J. Hare (2012), On trade wind cumulus cold pools, *J. Atmos. Sci.*, *69*(1), 258–280.